Observations of Stably Stratified Flow through a Microscale Gap

DANIEL VASSALLO,[a] RAGHAVENDRA KRISHNAMURTHY,[b] ROBERT MENKE,[c] AND HARINDRA J. S. FERNANDO[a,d]

[a] *Environmental Fluid Dynamics Group, Department of Civil and Environmental Engineering and Earth Sciences, University of Notre Dame, Notre Dame, Indiana*
[b] *Pacific Northwest National Laboratory, Richland, Washington*
[c] *Department of Wind Energy, Technical University of Denmark, Lyngby, Denmark*
[d] *Department of Aerospace and Mechanical Engineering, University of Notre Dame, Notre Dame, Indiana*

(Manuscript received 18 March 2020, in final form 5 October 2020)

ABSTRACT: This paper reports the findings of a comprehensive field investigation on flow through a mountain gap subject to a range of stably stratified environmental conditions. This study was embedded within the Perdigão field campaign, which was conducted in a region of parallel double-ridge topography with ridge-normal wind climatology. One of the ridges has a well-defined gap (col) at the top, and an array of in situ and remote sensors, including a novel triple Doppler lidar system, was deployed around it. The experimental design was mostly guided by previous numerical and theoretical studies conducted with an idealized configuration where a flow (with characteristic velocity U_0 and buoyancy frequency N) approaches normal to a mountain of height h with a gap at its crest, for which the governing parameters are the dimensionless mountain height $G = Nh/U_0$ and various gap aspect ratios. Modified forms of G were proposed to account for real-world atmospheric variability, and the results are discussed in terms of a gap-averaged value G_c. The nature of gap flow was highly dependent on G_c, wherein a nearly neutral flow regime ($G_c < 1$), a transitional mountain wave regime [$G_c \sim O(1)$], and a gap-jetting regime [$G_c > O(1)$] were identified. The measurements were in broad agreement with previous numerical and theoretical studies on a single ridge with a gap or double-ridge topography, although details vary. This is the first-ever detailed field study reported on microscale [$O(100)$ m] gap flows, and it provides useful data and insights for future theoretical and numerical studies.

KEYWORDS: Atmosphere; Boundary layer; Microscale processes/variability; Wind; Small scale processes

1. Introduction

Strong gusty winds associated with narrow mountain passages are known as gap winds, bottleneck winds, or funnel winds. Reed (1931) first discussed gap winds in the context of "climatic eccentricities" and "gale-force winds" observed in the Strait of Juan de Fuca. Arguably, they were neither the typical gradient nor katabatic winds, and appeared to be dominated by inertial, pressure gradient, and buoyancy forcing (Scorer 1952). The topographic window that allows such winds ranges from a simple col (gap) on a ridgeline (e.g., a depression or saddle on a mountain) to a sizable gap between two mountain peaks or a complex mountain pass with topographic incisions. Gap flows may lead to extreme weather events that endanger local populations, threaten existing infrastructure, and lead to unsafe conditions for aviation (Politovich et al. 2011). Past studies have investigated gap flows in a myriad of geographic regions such as the Strait of Juan de Fuca (Overland and Walter 1981; Colle and Mass 2000), the Strait of Gibraltar (Dorman et al. 1995; Scorer 1952), Howe Sound in British Columbia (Finnigan et al. 1994; Jackson and Steyn 1994), the Wipp Valley (Mayr et al. 2004; Weissmann et al. 2004; Marić and Durran 2009), and the Chivela Pass (Clarke 1988; Steenburgh et al. 1998). A comprehensive listing of studies theretofore is found in Table 1 of Pan and Smith (1999).

The archetypal stably stratified gap flow scenario occurs when fluid stratification impedes a flow's ability to scale an obstacle, thus causing gap-normal flow to converge at the entrance of a symmetrical gap incised into an otherwise uniform ridge, resulting in acceleration and a drop in pressure along the gap axis. This occurs because rising fluid parcels along the slope seek the path of minimum potential energy increase, which for a portion of the flow requires passing through the gap. The entrance pressure may not be recovered at the gap exit during flow diffluence, however, due to energy losses caused by fluid friction. This drop in pressure is a feature of the nonlinear gap flow regime defined by wave breaking and energy dissipation in the lee discussed by Zängl (2002), which is to be contrasted with the linear regime (no wave breaking) that displays small flow perturbations and no head losses (Saito 1993).

Gap flow dynamics of nominally two-dimensional (2D) mountains can be classified using the along-ridge gap width (W), cross-ridge length (L), and characteristic upstream velocity (U_0) scales. Although U_0 is in general a function of elevation z for atmospheric flows, in discussing canonical flows, a constant (characteristic) value is used for simplicity. Each of the aforementioned studies considers mesoscale gap flows ($W \geq 10$ km, $U_0 \sim 10\ \mathrm{m\,s^{-1}}$) with approach flow approximately parallel to the gap axis. Such flows are dominated by the Coriolis force, the criteria for which are the Rossby number $\mathrm{Ro} = U_0/fW \sim 1$, where $f \sim 10^{-4}\ \mathrm{s^{-1}}$ is the planetary vorticity (Overland 1984) and $\sqrt{\mathrm{Bu}} = Nh/fW < 1$, where Bu is the Burger number, N the representative buoyancy frequency, and h the ridge height (Trüb and Davies 1995; Sprenger and Schär 2001). Conversely, the microscale gap flows considered here are defined as those that are independent of Earth's Coriolis

Corresponding author: Daniel Vassallo, daniel.a.vassallo.4@nd.edu

DOI: 10.1175/JAS-D-20-0087.1

© 2020 American Meteorological Society. For information regarding reuse of this content and general copyright information, consult the AMS Copyright Policy (www.ametsoc.org/PUBSReuseLicenses).

force, for example, for the present microscale gap case of $W \sim O(100)$ m, $U_0 \sim O(10)$ m s^{-1}, $h \sim O(100)$ m, and $N \sim O(0.01)$ s^{-1}, leading to Ro $\sim O(10^3) \gg 1$ and $\sqrt{\text{Bu}} \sim O(100) \gg 1$. Such microscale flows could be important in wind engineering, where gap winds are perceived to be strong and favorable for wind turbine siting, notwithstanding the difficulties associated with increased turbulence, wind gusts, and possible lower winds under certain conditions. Microscale gap flows have been discussed by Saito (1993), Zängl (2002), and Gaberšek and Durran (2004) for the case of ridge-normal flow and by Sprenger and Schär (2001) for along-ridge flow, although flow sensitivity to topography and background stratification continues to stymie the development of a broadly applicable theory.

This paper analyzes field observations of flow through a microscale gap located in one of the two parallel ridges studied in the Perdigão field campaign that took place from 1 May to 15 June 2017 (Fernando et al. 2019). Perdigão was an EU–U.S. project designed to study winds in nominally parallel double-ridge topography, with the aim of eliciting dynamical and thermodynamical processes of microscale flow in complex terrain while contributing to the development of microscale models for wind-resource prospecting and mapping. One of the ridges has a microscale depression (gap), and therefore a subexperiment was conducted by deploying a dedicated set of instruments within the overall Perdigão campaign. To our knowledge, this is the first reported comprehensive microscale gap flow field investigation. Section 2 presents theoretical preliminaries that are useful for explaining the observations, and section 3 discusses the gap flow experiment. Results are given in section 4 with a brief discussion in section 5. Concluding remarks are made in section 6.

2. Theoretical preliminaries

Smith (1980), Baines (1987, 1998), Whiteman (2000), Chow et al. (2013), and Blumen (2016), among others, provide extensive reviews on the state of knowledge on flow over topography. For the simple (no-gap) case of deep, uniform normal approach flow of velocity U_0 and buoyancy frequency N toward a single 2D mountain of height h, the sole governing parameter is the nondimensional mountain height $G = Nh/U_0$, where U_0/N is the stratification length scale. $0 < G \ll 1$ represents relatively small topographically induced flow perturbations, for which linear theories are applicable. In laboratory studies, Baines and Hoinka (1985) identified $G < 0.5$ as the linear regime, whence vertically propagating internal waves of wavelength $\sim U_0/N$ are accompanied by accelerated winds over the lee slope, consistent with earlier theoretical analyses (Queney 1948; Klemp and Lilly 1975).

Drastic flow alterations occur when $G > 0.5$. For example, according to Baines and Hoinka (1985), trapped lee waves and partial upstream blocking arise when $0.5 < G < 2$ whereas superposition of upstream columnar disturbances leads to blocked flow for $G \geq 2$ (Baines 1979). Larger G [$>O(1)$] also encompasses a nonlinear wave-breaking regime, analysis of which has been accomplished using hydraulic and shallow flow models (Long 1952, 1953; Houghton and Kasahara 1968; Pan and Smith 1999) or full nonhydrostatic simulations. According to Baines and Hoinka (1985), stagnant rotors occur downstream of the ridge alongside lee waves, which progressively steepen and eventually overturn when $G \geq 1.5$. With increasing G, flow passes both over and under these rotor structures while spreading horizontally toward and over the obstacle (reverse flow in the lee), leading to shear and critical layers. These laboratory flows showed only little sensitivity to obstacle shape, although numerical simulations indicate that obstacle shape is important for certain flow regimes (Gaberšek and Durran 2004).

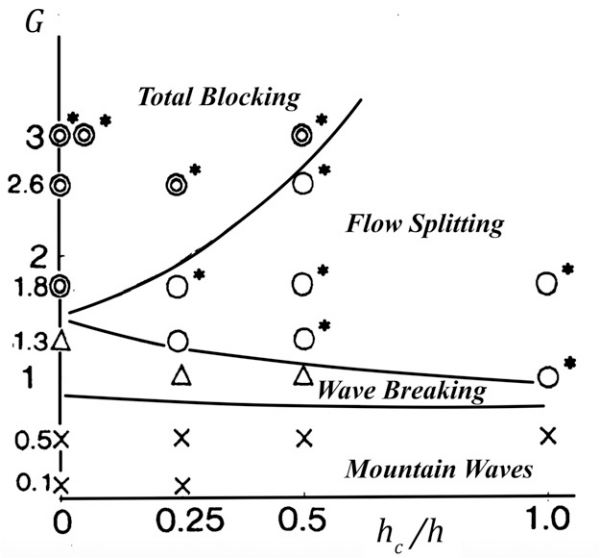

FIG. 1. Adapted from Fig. 11 of Saito (1993), the figure depicts flow regimes found for flow approaching a mountain with a gap via nonlinear simulations. Double circles, open circles, triangles, and crosses denote total blocking, flow splitting, wave breaking, and only mountain waves, respectively. Curved lines show the critical curves of G that divide the flow regimes. Asterisks indicate the cases in which reverse wind occurs.

Naturally, when a gap of height h_c, (along-ridge) width W, and (cross-ridge) length L is present atop a single mountain, additional governing parameters enter the problem; these include the nondimensional gap height h_c/h, width W/h, length L/h, and the gap geometry (a list of topographic parameters is given in Table A1 alongside a definition diagram in Fig. A1). Earth's rotation may be excluded considering a microscale gap. Laboratory experiments performed by Baines (1979) with a full-depth gap ($h_c/h = 1$) indicate that gap effects are localized for $G > 2$. In this regime, lateral flow deflection and upstream blocking occur below the dividing streamline height z_s ($z_s < h$) which depends on G and W/h. Saito (1993) numerically simulated ridge-normal flow over a mountain ridge modified by a series of peaks and passes (gaps) along the ridgeline. Comparison of linear solutions based on Smith (1980) with full nonlinear numerical simulations allowed for separation of linear and nonlinear flow effects on a h_c/h–G regime diagram (Fig. 1). Mountain waves, wave breaking, flow splitting, and total blocking were identified as ensuing key processes. Zängl (2002) attempted to exclude 2D internal waves excited by the gap periodicity of Saito (1993) by considering a level gap.

While the specifics vary, past studies exhibit accelerating winds along the gap axis in the linear regime [$G < O(1)$]. Zängl (2002) identified flow confluence at the gap entrance as well as dispersive internal waves that radiate from the ridge and intersect aloft the gap axis. Therefore, the gap width has an influence on the flow in the linear regime while the lee wind speed, except for very narrow gaps ($W/h_c \ll 1$), was found to be lower than that over the neighboring unmodified mountain ridge.

The simulations of Gaberšek and Durran (2004) considered a full-depth gap in a ridge of finite length, allowing flow around the lateral edges of the mountain and arguably providing a better representation of natural flows. No enhancement of gap flow speed was observed for small G. A mountain wave regime with partial upstream blocking appeared at intermediate G ($\sim$1.5). This regime exhibited highest wind speeds at the gap exit, lee wave formation and breaking on the lee slope, and potential for a hydraulic jump following a separated lee jet. Further, negative pressure perturbation in the lee induced flow subsidence from above. When friction and Earth's rotation were added to the simulation, the greatest positive relative gap flow enhancement was achieved for $G \sim 5$ (Gaberšek and Durran 2006).

According to Zängl (2002), both lee waves and upstream blocking are present in the nonlinear regime ($G > 2$). Upward wave propagation is limited due to low-level wave breaking, and the gap flow is governed by the pressure drop across the gap induced by the high-drag state of flow over the ridge. Flow over the ridge and that through the gap were decoupled, and flow was insensitive to the gap width. According to Gaberšek and Durran (2004), wave-induced downward momentum flux both over the lee slope and within the gap region is also an important factor (alongside the pressure drop) for gap flows. Their $G = 5$ case was in the fully blocked regime, with the highest velocity at the gap entrance due to convergence and pressure gradient effects. Quite interestingly, the fraction of the total approach flow passing through the gap was relatively independent of G across all flow regimes.

In the partially blocked regimes, fluid parcels above the dividing streamline height (z_s) have sufficient kinetic energy to rise and flow over the mountain whereas those below z_s are either stagnant or deflected and flow around the mountain. Sheppard (1956) estimated z_s using simple energy arguments as

$$\frac{U_0^2(z_s)}{2} = \int_{z_s}^{h} (h - z) N^2(z)\, dz, \tag{1}$$

where

$$N^2 \approx \frac{g}{\theta_e(z_s)} \left(\frac{d\theta_e}{dz} \right), \tag{2}$$

z is the elevation (in this case, above upstream ground level), g the gravitational acceleration, and θ_e the virtual potential temperature. For the simplest case of constant N and U_0, Eq. (1) becomes $z_s/h = 1 - G^{-1}$, requiring $G > 1$ for the existence of the dividing streamline. The work of Sheppard (1956) has been subject to voluminous later studies, a brief review of which is found in Leo et al. (2016).

The studies discussed above are for a single mountain, but the interest here is a double-ridge configuration with a gap in one of the ridges. Therein a basic flow would be that over a double-ridged mountain without a gap, which has been shown to differ from a single mountain case, especially with regard to lee wave generation. An additional dimensionless parameter comes into play: the dimensionless valley width V/h (assuming ridges of equal height h; V is the valley width). Linear interference theory (Stiperski and Grubišić 2011) suggests that maximum constructive interference occurs for $V/\lambda_s = n, n \geq 1$ (λ_s is the intrinsic wavelength for a single ridge and n an integer), whereas maximum destructive interference occurs for $V/\lambda_s = (2n - 1)/2$. Grubišić and Stiperski (2009), however, illustrated that trapped waves adjust to the topography and preferentially fit to become an integer fraction of the valley width, therefore leading to subsidence in the lee of the downstream ridge. Double-ridge towing tank experiments of Gyüre and Jánosi (2003) showed that above-ridge flow dips into the valley when $G = 0.5$ (linear regime) and flows over the valley when $G = 2$ (nonlinear regime). The existence of a downstream ridge not only reduces wave amplitude over the valley (Stiperski and Grubišić 2011), but also decreases both the wavelength and amplitude of the lee wave downstream of the downstream ridge when $G > 1$ (Gyüre and Jánosi 2003). The double-ridge configuration is expected to both drop the height of the elevated inversion above the upstream ridge (if an inversion exists) and reduce upstream blocking compared to that of a single ridge (Stiperski et al. 2017). Additionally, Stiperski and Grubišić (2011) showed that, under no-slip conditions, the surface wind speed in the vicinity of the upstream ridge is maximized at the ridge's apex. Stiperski et al. (2017) conducted towing-tank experiments with stratification in the form of an inversion for both single and double-ridge cases, and developed flow regime diagrams. Differences were noted with previous studies on detailed aspects of flow. The ratio of obstacle heights and valley width were found to play important roles for lee wave characteristics as well as the transition between different flow regimes (e.g., trapped lee waves, rotors, hydraulic jumps, flushing of the valley). We have found no previous studies detailing flow over two ridges, one of which contains a gap.

Note that the double-ridge configuration is an intermediate case between a single ridge and a series of periodic hills, the latter being a metaphor of a two-ridge case where one ridge is affecting the other. The case of uniform stratified flow of velocity U_0 and buoyancy frequency N over periodic hills with ridge separation λ (or horizontal wavenumber $k_1 = 2\pi/\lambda$) has a well-known linear solution (Gill 1982). Accordingly, vertically propagating waves are possible when the vertical wavenumber k_3 is real, i.e., $k_3^2 = k_1^2[(N/k_1 U_0)^2 - 1]^2$, or $N\lambda/U_0 > 2\pi$. Under these conditions, the windward (lee) side of the hill has a positive (negative) pressure perturbation, thus providing a favorable pressure gradient for enhancing the gap flow. This condition is achieved for the present case when $(Nh/U_0)(\lambda/h) > 2\pi$, or $G > 1$, considering $\lambda/h \approx 6$ ($\lambda = V \approx 1.5$ km, $h \approx 250$ m). In the opposite limit, $(N\lambda/U_0) < 2\pi$ or $G < 1$, no such favorable pressure gradient exists, and the system lacks one of the mechanisms that enhances gap flow amplification.

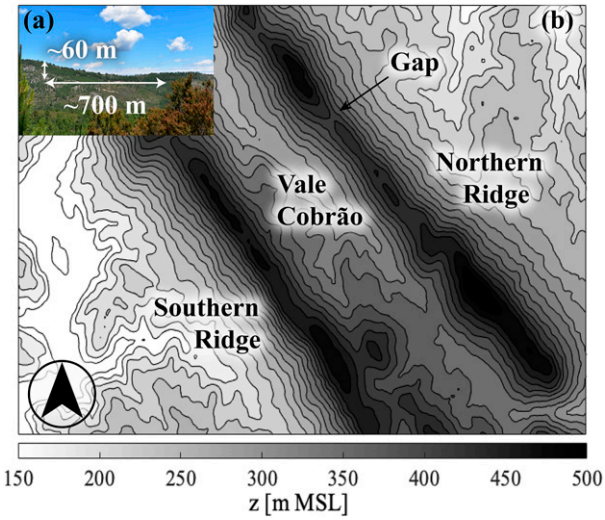

FIG. 2. (a) A photograph of the gap in the northern ridge, looking east from the valley. (b) Contour plot of the campaign topography. The gap can be seen in the northern portion of the northern ridge. Contours demark elevation changes of ~20 m.

3. The Perdigão campaign

a. Local topography

The Perdigão campaign was conducted in Vale do Cobrão, Portugal (Fig. 2), located approximately 23 km southwest of Castelo Branco and just over 100 km east of the Atlantic coast. The experiment was named after a small town (Perdigão) just southwest of Vale do Cobrão, which was chosen due to its unique topographical features. It extends over 4 km from northwest (NW) to southeast (SE), with its width varying between 1.4 and 1.8 km. Two nearly parallel ridges delimit the valley, both running NW to SE. The one to the north is henceforth referred to as the northern ridge and that to the south the southern ridge. Both rise approximately 250 m above the surrounding topography, with the southern ridge rising (on average) ~25 m above its northern counterpart. The campaign domain contains farmland and dense vegetation that rises approximately 10 m above ground level (AGL). The area immediately surrounding the ridges consists primarily of flat land and rolling hills, with small towns and farmland interspersed. One 2 MW wind turbine was operational on the southern ridge. For further details about local topography and climatology, see Fernando et al. (2019).

Our investigation focuses on the microscale gap in the northern ridge shown in Fig. 2. Although the ridge never truly levels off at its apex and has undulations along the ridgeline, the gap is clearly distinct from its surroundings, extending approximately 700 m wide, 60 m deep, and 100 m in length, with somewhat irregular and pitted edges. The NW edge of the gap rises at a much steeper slope than the SE edge, ascending ~25 m above the latter, causing the gap to be somewhat laterally asymmetrical. The normalized gap height (h_c/h) is approximately 0.25. Given the NW–SE orientation, northeasterly and southwesterly winds run normal to the ridge. While 3-yr climatology based on 40 m tower measurements on the southern ridge show primarily northeasterly and southwesterly wind patterns (Vasiljević et al. 2017), daily climatology at lower levels can be strikingly different and highly variable (Fernando et al. 2019).

b. Instrument siting and specifications

Vale do Cobrão and its surrounding region were outfitted with 49 meteorological towers placed in a grid formation. Three rows of towers ran parallel to the valley axis and two rows ran perpendicular (Fernando et al. 2019, their Fig. 5). The towers were outfitted with a total of 186 three-component sonic anemometers at various heights as well as a host of other sensors. The region surrounding the gap was specifically instrumented to provide a comprehensive view of the flow upstream, downstream, and within the gap (Fig. 3a). Five meteorological towers (tnw12–16, Fig. 3a) were located on the NE face (outside the valley) of the northern ridge to provide flow speed and direction at various heights up to 28 m AGL. Tnw12 was the topmost of these towers and was located at the outer, northeastern gap entrance. Three 20 m towers were located within the gap, one in the gap center (tnw11, Fig. 3a) and one at each edge (rne06–07, Fig. 3a), with sonic anemometers at 10 and 20 m AGL. Towers also continued down the SW side (inside the valley) of the northern ridge, starting at the center of the gap and continuing through the SW face of the southern ridge (towers in the valley are not shown). One meteorological tower (tnw10, Fig. 3a) at the gap southern exit had sonic anemometers at 10, 20, 30, 40, and 60 m AGL. All other towers within the valley captured the valley flow at lower levels (≤20 m AGL) and provided auxiliary information for the study.

A synchronized triple Doppler lidar system (TL1, 2, 3, Fig. 3b) was used to probe flow along the gap cross section and within the valley (downstream of the gap during northeasterly flow). This is a novel implementation of the triple Doppler lidar technique to Halo Photonics Streamline XR lidars (Pearson et al. 2009; Wang et al. 2016; Newsom and Krishnamurthy 2020). The lidars were automated to achieve a common (yet moving) intersection point, which provided (along-beam) radial wind velocity in three directions at this location, from which the full velocity vector at the intersection point can be retrieved without making often-invoked homogeneity assumptions about the flow (Fernando et al. 2019). Two of the lidars (TL1 and TL2, Fig. 3a) were located within the valley and another (TL3) on the northern ridge just SE of the gap. The three lidars performed coordinated range–height indicator (RHI) scans, with all three beams intersecting at a given point that could be rapidly traversed vertically to obtain "virtual towers." These towers measure vertical profiles of wind speed and direction from near surface to 500 m AGL at a given location, then relocating to a different point to begin scanning for another virtual tower (Calhoun et al. 2006; Newsom et al. 2015; Lundquist et al. 2017; Fernando et al. 2019; Newsom and Krishnamurthy 2020). An unsynchronized dual Doppler lidar system was also utilized to measure the flow northward of the northern ridge (upstream of the gap during northeasterly flow). One lidar (DL1, Fig. 3a) was located on the northern ridge just NW of the gap, while the other (DL2) was located ~600 m NE of the gap. The virtual tower measurements by DL1 and 2 were not synchronized by a master

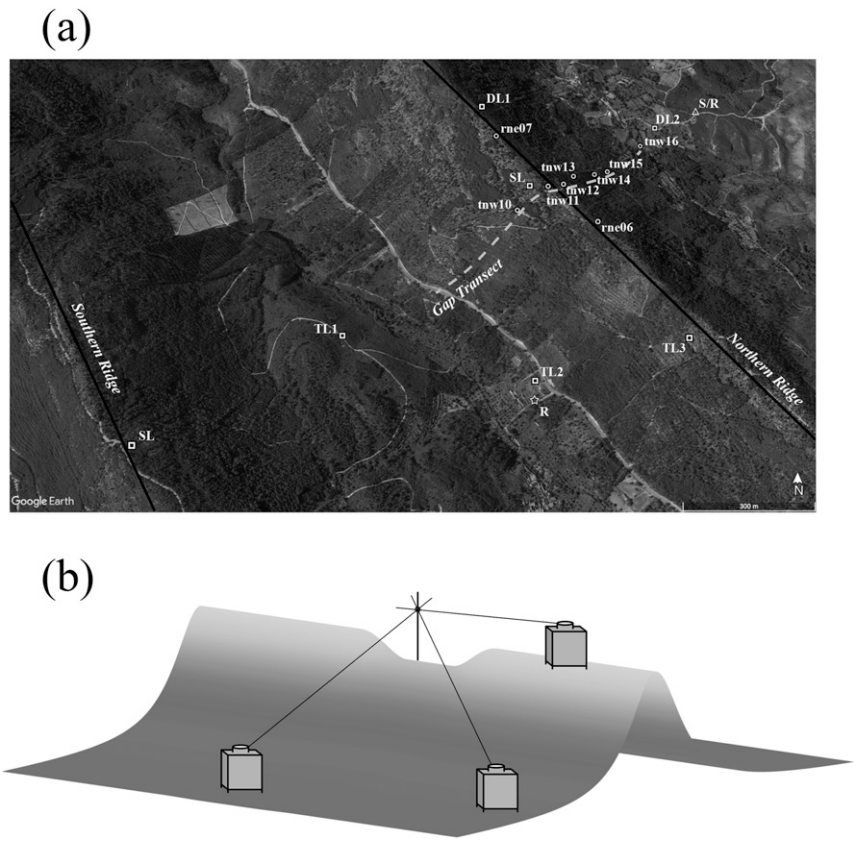

FIG. 3. (a) Instrumentation used to classify flow in the vicinity of the gap. Circles, squares, triangle, star, black lines, and gray line denote meteorological mast, lidar, sodar/RASS, radiosonde, ridge locations, and the gap transect, respectively. See section 3b for further details. (b) Illustration of the triple Doppler lidar setup with beams directed at one point on a virtual tower within the gap. Eight virtual towers spanned the width of the gap, seven were located upstream, and three were downstream.

controller, while the measurements from TL 1, 2, and 3 were synchronized by a master controller. The uncertainty (generally below 2%) of synchronized versus unsynchronized measurements for a complex terrain site is a topic of current research but is not expected to affect the conclusions from this study (Lundquist et al. 2015; Choukulkar et al. 2017; Newsom et al. 2017).

During Perdigão, although each lidar range gate was set to 18 m, overlapping beam measurements were performed every 3 m along each line of sight. This helped in accurately selecting the closest range gate to the gap location, aided by high-resolution topography data available from an aerial survey (Mann et al. 2017). The vertical resolution during post-processing was chosen to be 10 m. For this study, eight virtual towers were performed along the gap cross section (typically spaced just over 100 m apart, with the outermost virtual towers just outside of the gap edges), with each profile taking roughly 1 min to complete. Therefore, at minimum each 30-min averaged profile has measurements from three virtual towers for a given location. Further discussions are provided in Fernando et al. (2019).

A sonic detection and ranging (sodar)/radio acoustic sounding system (RASS) (S/R, Fig. 3a; Scintec MFAS), located approximately 800 m NE of the gap, provided 30-min averaged velocities up to 400 m AGL. Upper-air information during the gap experiment was determined via radiosonde launches within the valley (R, Fig. 3a) conducted every 3 to 6 h. Additional scanning lidars (e.g., SL in Fig. 3a) were placed at select locations along each ridge to provide cross-sectional scans of radial wind velocity (U_r) normal to the valley axis (Menke et al. 2019). For a full list of instrumentation deployed and details about data availability, see Fernando et al. (2019).

c. Flow direction

Low-level winds showed significant variability with time. Therefore, for obtaining fundamental insights on this double-ridge configuration, periods with low-level approach flow [<250 m AGL at the S/R location, or <500 m above mean sea level (MSL); S/R located ~250 m MSL] approximately normal to the ridge axis (i.e., northeasterly and southwesterly flows) were selected for analysis. Moreover, because southwesterly flow is modified by the valley and the southern ridge before reaching the gap, the analysis was further restricted to northeasterly approach flow (defined as the mean gap-level flow of 45° ± 15°). For these conditions, the S/R provided upstream

wind speed and direction (~10 m vertical resolution) up to 400 m AGL. Note that lidar scans and tower and S/R measurements were largely continuous and the data were voluminous. Nevertheless, the scope of the study (i.e., approximately ridge normal, continuously stably stratified, weakly sheared flow over the gap height with adequate quasi-stationarity during the 30-min averaging period) permitted only limited data to be used for this study. These restrictions were necessary for the generality of the conclusions of the study.

Considerable upstream flow turning was occasionally observed from ground level to ridge elevation, likely due to topographically induced lateral flow deflection during stratified periods. As a result, specification of upstream flow conditions was based on flow over the gap height, i.e., $0 \le z^*/h_c \le 1$, where h_c is again the gap height defined as the distance from the gap base (~435 m MSL), to the highest (ridge) point at the gap's NW edge (~495 m MSL), and z^* is the vertical elevation above the gap base (Fig. A1). Thus, for the cases selected, within this ~60 m vertical slice, flow approached normal to the ridge.

d. Flow stability

Atmospheric stability in the surface layer is typically expressed in terms of a standard vertical distance normalized by the Monin–Obukhov length scale or a suitably defined gradient Richardson number (Kaimal and Finnigan 1994). Nonetheless, the very foundations of the Monin–Obukhov theory fail in complex terrain due to a lack of horizontal homogeneity, while use of the gradient Richardson number poses challenges as it varies with height and measurement resolution. As discussed in section 2, the commonly used governing dimensionless parameter for the problems of stably stratified flow over hills is $G = Nh/U_0$, but it does not account for the vertical variation of N and U_0. To address this complication, three values of G were computed. The first, G_c, is found by calculating 30-min averaged upstream G (using S/R measurements to get N and U_0) in 10 m vertical increments and averaging the ensuing values over the gap height. G_t is found in the same way, but averaging is taken from the ground (>40 m AGL, which is the lowest height consistently measured by the S/R) to the ridge height, providing flow information below the gap base (and potentially below the dividing streamline). The third was an equivalent value, G_e, calculated based on simple energetics. Here, the potential energy of a fluid parcel lifted through the measured environmental stratification up to the ridge height was calculated. The equivalent (uniform) buoyancy frequency N_e that would yield this potential energy during the same movement may be used together with the ground level approach velocity to calculate G_e (the average U_0 from 40 m AGL to ridge height was taken for this study due to questionable reliability of S/R data near the ground). The calculation of N_e followed Eq. (2), with $d\theta_e/dz$ taken from upstream ground level to ridge height:

$$\frac{U_0^2}{2} = \int_{z_s}^{h} (h - z)N^2(z)\,dz \approx h^2 \int_0^1 (1 - \xi)N^2(\xi)\,d\xi = N_e^2 h^2 \int_0^1 (1 - \xi)\,d\xi = \frac{N_e^2 h^2}{2}, \tag{3}$$

where $\xi = (z - z_s)/(h - z_s)$ and z_s ($<h$) again is the upstream dividing streamline height. Thus, the parameter $G_e = N_e h/U_0$ is an indicator of whether the fluid parcels near ground level (40 m AGL at the S/R location, again using N_e and U_0 found by the S/R) have sufficient energy to rise to ridge height without experiencing splitting or flow reversal. These upstream effects are brought about by division of flow at z_s to generate two layers, a top layer flowing above the obstacle and a bottom layer flowing around the obstacle (splitting) with the potential for recirculation normal to the obstacle (flow reversal), as described in Brighton (1978), Boyer et al. (1989), and Lin et al. (1992).

TABLE 1. Study periods with corresponding G values.

Date and time	Regime	G_c	G_t	G_e
0700–0730 UTC 24 May	1	0.3	0.7	0.7
0100–0130 UTC 23 May	1	0.8	6.6	1.3
0800–0830 UTC 31 May	2	1.3	1.5	1.5
0730–0800 UTC 1 Jun	2	1.4	1.6	1.2
0700–0730 UTC 31 May	3	2.5	10.5	4.3
0230–0300 UTC 12 Jun	3	6.5	17.7	13.8

It was of interest to evaluate how field observations compare with previous numerical and theoretical results obtained using idealized flow configurations. Thus, the time periods selected for analysis have G values (specifically G_c) comparable to those considered in previous studies. These ranged from small ($G_c \approx 0.3$; brought on by mild stratification, high wind speeds, or a suitable combination thereof) to large ($G_c \approx 6.5$; brought on by strong stratification, low wind speeds, or a suitable combination thereof) nondimensional heights (cf. qualitatively to Fig. 1). While so doing, it was necessary to compromise the requirements of uniform stratification, weak vertical shear and northeasterly flow to some degree, and the best cases meeting our requirements were selected. Unstable cases ($N^2 < 0$, averaged over the gap height) were removed from consideration.

e. Periods chosen

Nearly neutral conditions were rare and typically occurred during morning transition periods (from stable nocturnal conditions to daytime convective conditions). Two particularly interesting cases were the morning transition period at 0700–0730 UTC 24 May with $G_c = 0.3$, and at 0100–0130 UTC 23 May with $G_c = 0.8$ (local time = UTC + 1 h). This corresponds to the linear mountain wave regime of Saito (1993), shown in Fig. 1. On the other hand, stably stratified periods were more prevalent throughout the intensive operational period (IOP) of the Perdigão campaign. Upstream conditions between 0730 and 0800 UTC 1 June and between 0830 and 0900 UTC 31 May showed northeasterly flow with $G_c = 1.4$ and $G_c = 1.3$, respectively, comparable to the mountain wave regime analyzed by Gaberšek and Durran (2004) and the wave-breaking/flow splitting regime of Saito (1993). Another case, between 0700 and 0730 UTC 31 May, had $G_c = 2.5$, just smaller than the $G \approx 3$ conditions investigated in various previous studies (Saito 1993; Zängl 2002; Gaberšek and Durran 2004) and corresponding to the total blocking regime of Saito (1993). The most stable period fitting the inflow requirements occurred between 0230 and 0300 UTC 12 June, with $G_c = 6.5$, again belonging to the total blocking regime of Saito (1993).

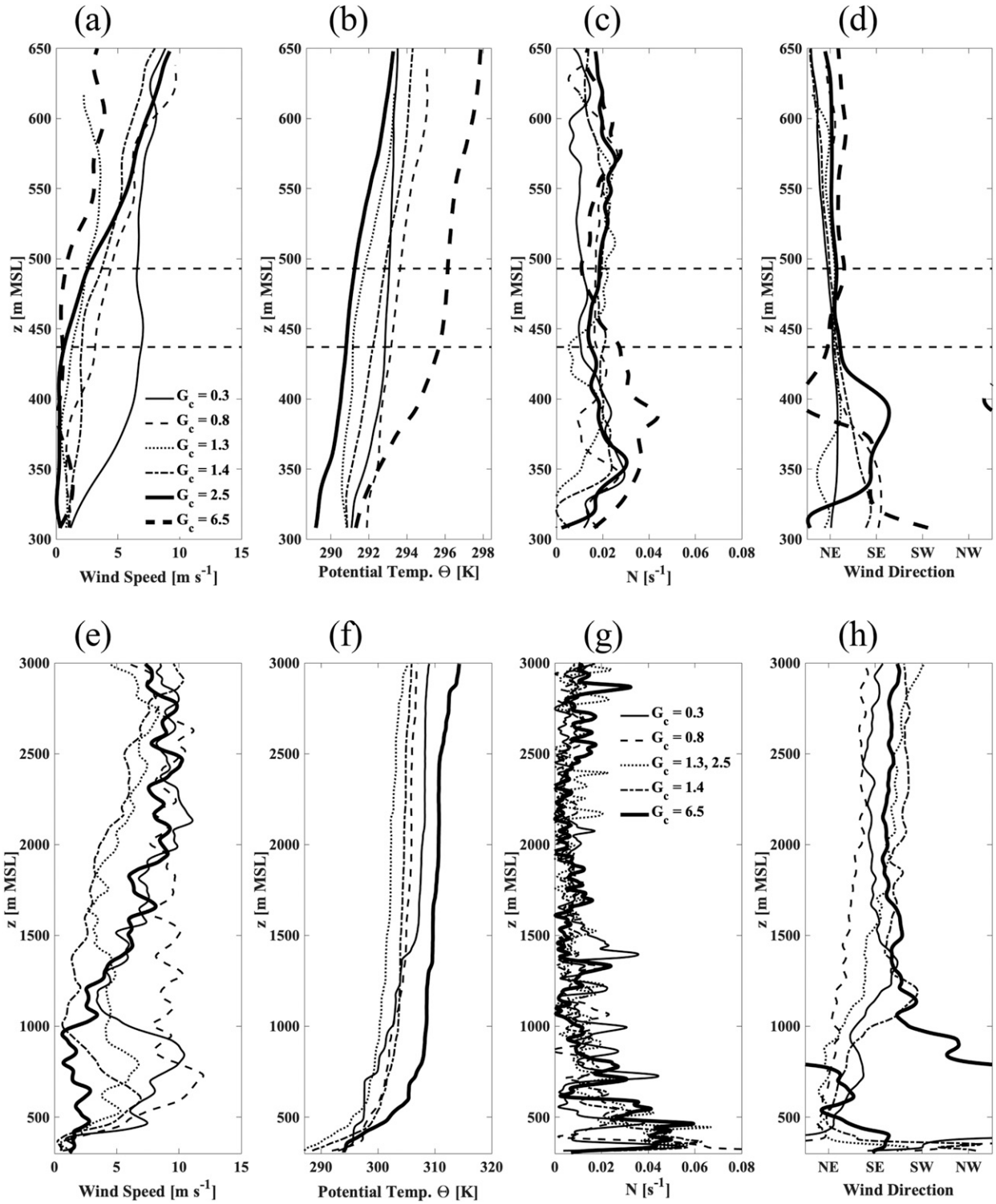

FIG. 4. (a),(e) Wind speed; (b),(f) potential temperature; (c),(g) buoyancy frequency N; and (d),(h) wind direction for (top) sodar/RASS (S/R) measurements upstream (NE of the gap) and (bottom) the closest radiosonde launch (marked R in Fig. 3a). Horizontal dashed lines in the top row denote the gap region. The periods of $G_c = 1.3$ and $G_c = 2.5$ are represented by a single radiosonde launch [dotted lines in (e)–(h)] as they occur on the same morning.

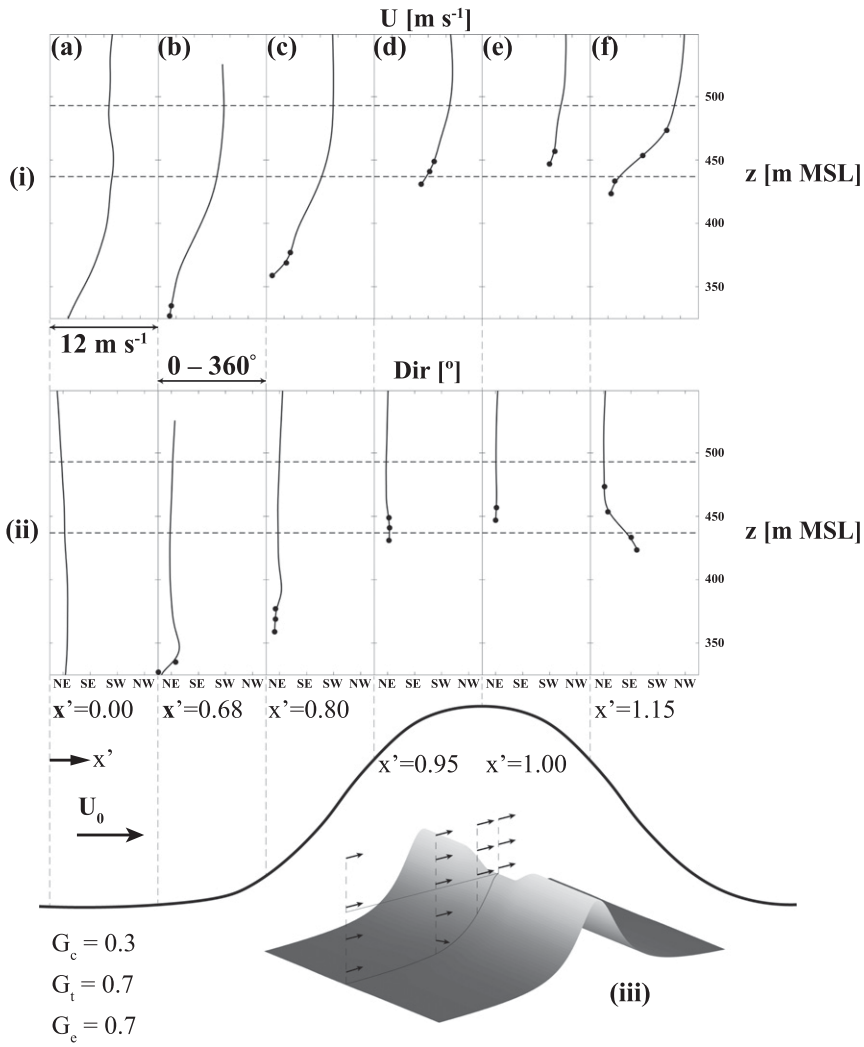

FIG. 5. Case 1: spline interpolated flow (top) speed U and (middle) direction (Dir) (a)–(c) on the windward slope as well as at the gap (d) entrance, (e) center, and (f) exit, when G_c = 0.3. Depicted flow moves left to right, indicated by the arrow below U_0. Filled in circles denote tower measurements. (bottom) A case-specific flow schematic. The solid black line below the middle row provides an illustrative view of the topography along the gap transect. x' is the normalized distance along an axis originating from the S/R location (beginning of the x' arrow) and extending southwestward through the center of the gap. The distance from the S/R to the gap (~800 m) is the normalizing variable.

Table 1 shows the study cases alongside their respective G values. In all, six different cases were identified which satisfy the background conditions of interest. The entire dataset is available in the repositories mentioned in Fernando et al. (2019) for the benefit of future studies.

4. Results

The upstream S/R flow velocities for each of the six cases are shown in Figs. 4a–d, alongside the closest radiosonde measurements taken inside the valley (Figs. 4e–h). Note the approach flow at the gap height is variable but generally northeasterly, with high-G cases displaying lower wind speeds and higher velocity variability at gap height. Flow observations at different G_c are described below. Periods described are relatively stationary, with a majority of wind speeds remaining nearly constant (to within 0.3 m s^{-1}) throughout the period. Parameter x' (in Figs. 5, 7, 9, 11, 13, 15, and 18) indicates the normalized distance along the northern ridge cross-sectional axis originating from the S/R location and extending southwest through the center of the gap. The distance from the S/R to the gap center (~800 m) is the normalizing variable.

a. Case 1: Low G

The case with the lowest G value (G_c = 0.3) occurred during the morning transition period between 0700 and 0730 UTC

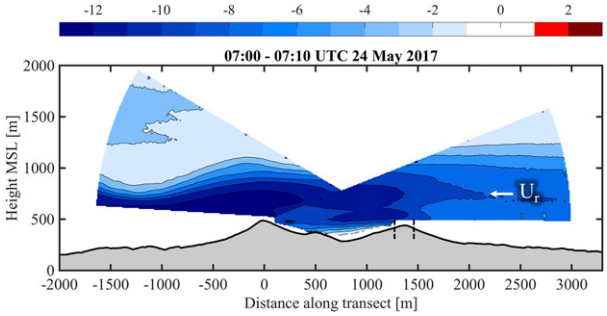

FIG. 6. Case 1: averaged cross-ridge lidar measurements (gap on the right ridge) during the first 10 min of the time period when G_c = 0.3. Blue (negative U_r) denotes flow from right to left, while dark red (positive U_r) denotes flow moving left to right. Gap entrance (right) and exit (left) are denoted by the vertical dashed lines adjacent to the peak of the right ridge. White arrow indicates incoming flow direction at gap height. For details see Menke et al. (2018).

24 May (sunrise at 0703 UTC). Winds approaching the gap were nearly northeasterly and relatively strong [$\sim$6.5 m s^{-1}; Fig. 5(i)a]. Dual lidar and tower measurements upstream of the gap axis display low-level northeasterly flow at the windward foothills [Figs. 5(ii)b,c], with little upstream flow deflection, indicating flow ascension and acceleration along the slope. Maximum acceleration ($\sim 1.5U_0$) was observed $\sim 1.5h_c$ above the gap base (Fig. 17; z^* again is the vertical elevation above the gap base), while flow direction at the gap height remained northeasterly through the gap exit. Figure 6 shows the images of RHI velocity scans by the two scanning lidars (SL) located on the northern and southern ridges, depicting U_r in the SW–NE plane (with $\sim$35 m measurement resolution). Since the approach flow is northeasterly, the lidar flow construct shown is a good approximation of the actual flow, although lidars only capture the along-beam velocity. Note the velocity amplification as flow approaches and passes through the gap, from about 6–7 to 8–10 m s^{-1} [Figs. 5(i)a–f]. There was no appreciable change of direction along the slope or through the gap, except at the gap exit where south/southeasterly valley flow was observed [Fig. 5(ii)f] with velocity $U \sim 1$ m s^{-1}. Xu and Yi (2013) studied recirculation behind a forested double-hill configuration and found that recirculation in such systems is governed by the mountain height h and half length l. Accordingly, for $h/l < 0.8$ sporadic reversed flow occurs. This is consistent with the present case where $h/l \approx 0.3$. Linear mountain waves are expected for $G < 1$ with a horizontal wavelength $\sim$1 km above the ridges (Fig. 1). This is on the same order as the stratification length scale $U_0/N \approx 850$ m, which is the wavelength expected from linear theory for a single mountain. It is noteworthy that in the laboratory experiments of Gyüre and Jánosi (2003) with a double-ridge and $G \approx 0.4$ (closest to our case) the flow passed over the topography with some weak wave structures aloft and weak flow in the valley. This is consistent with the lidar images shown in Fig. 6 where the wave appears to have fit to the topography (Grubišić and Stiperski 2009), although the wave downstream of the trailing obstacle appears to have larger amplitude than those in the laboratory studies.

Figure 7 shows the case of $G_c = 0.8$. In this case, G_e (1.3) and particularly G_t (6.6) are significantly larger, indicating considerable low-level stratification (below 360 m MSL, Fig. 4c) and low upstream wind speeds below the gap base (Fig. 4a). Low-velocity flow within this region of higher stratification does not have enough kinetic energy to ascend the hill and thus deflects laterally to bypass the hill. This is evident from low-level northwesterly and southeasterly flow in Figs. 7(ii)a–c.

From the gap level to 800 m MSL, upstream flow is northeasterly and continues as such until reaching the lee of the hill. The low to moderate G_c leads to a weaker acceleration with a maximum velocity of $\sim 1.3U_0$ (Fig. 17) within the gap. Unlike the parabolic normalized velocity profile observed for $G_c = 0.3$ (Fig. 17), one can begin to distinguish flow within the gap (with mild acceleration) from that above. A nearly stagnant recirculation region was evident which extended just above canopy height at the lee tower location (Fig. 7). Waves, while expected (section 2), were not clearly discernible in the lidar profile (Fig. 8).

b. Case 2: High G

Figure 9 shows the case of a large G_c (6.5), where flow above 1000 m MSL is southerly (Fig. 4h) but approach flow is approximately northeasterly because of topographic steering induced by the ridge (Fernando et al. 2019). High G_t (17.7) and G_e (13.8) reveal strong stratification within the lower air column, consistent with the nearly stagnant upstream flow observed below ridge height [Figs. 9(i)a–c]. Low-level approach flow has an along-ridge deflection to the southeast. However, unlike in case 1, canopy-level flow at the foothills veers southwesterly and is nearly stagnant [Fig. 9(ii)], indicating a zone of upstream flow blocking at low levels. As the flow reaches the gap entrance, the layer just above the gap base accelerates as it passes over the ridge, with in-gap amplification of about 6–7 times the upstream approach velocity (Fig. 17). Similar to the case study described in Mayr et al. (2004), flow in the lee of the gap continues without entering the valley (Fig. 10; the scanning lidar on the northern ridge was not functioning at this time), being separated from the in-valley flow by a strong temperature gradient at the ridge height (Fig. 4f).

The schematic in Fig. 9(iii) is based on lidar and tower observations. The scanning lidar on the southern ridge depicts the absence of wave activity above the valley, as flow is in the nonlinear regime (Gyüre and Jánosi 2003). Distinct flow layers are apparent, particularly at the ridge height where there is a nearly stagnant shear layer between valley flow and northeasterly flow passing over the ridges (Fig. 10). These observations are consistent with laboratory findings for strongly stratified cases ($G > 2$) that showed formation of shear layers in the proximity of the ridge, a thin layer of possible flow reversal at the ridgetop, and recirculating flow in the lee (Baines and Hoinka 1985). Further, a shear layer between valley and above-ridge flow is expected for double-ridge topographies in the nonlinear regime [$G > 1$ in Gyüre and Jánosi (2003)]. Both Baines (1998) and Saito (1993) showed that upstream blocking occurs below the dividing streamline for $G > 2$, whereas fluid above the dividing streamline flows over the ridge. As was described by Stiperski et al. (2017), however, the double-ridge topography is expected to lead to less upstream blocking

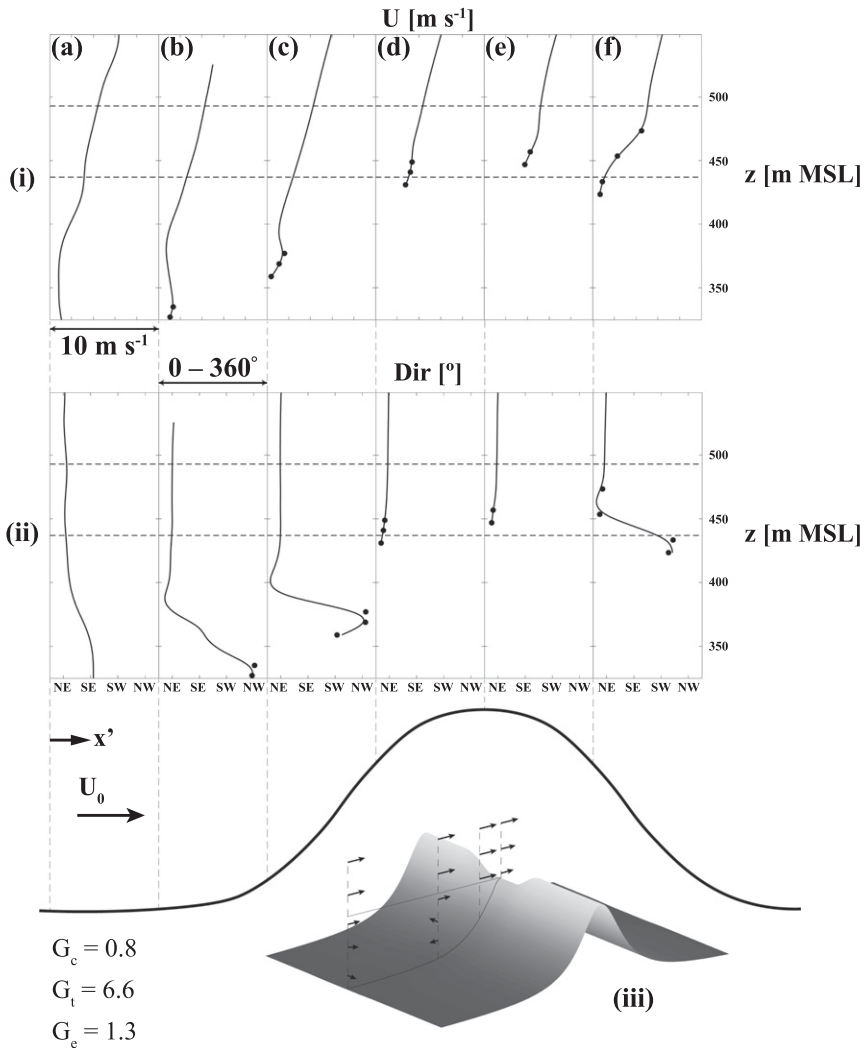

FIG. 7. Case 1: as in Fig. 5, but for the period with $G_c = 0.8$.

compared to a single ridge. Our observations are broadly consistent with these studies.

The second high-G case ($G_c = 2.5$) has similar characteristics to the case just described, and details can be seen in Figs. 11 and 12 . Both G_t (10.5) and G_e (4.3) were large, indicating considerable low-level stratification which, combined with nearly stagnant upstream flow speed, led to southeasterly flow deflection (Fig. 11). Once again, the gap flow remained approximately ridge-normal throughout the gap passage. Acceleration within the gap generated flow velocities up to $\sim 2.7U_0$ within the gap (Fig. 17). Mild recirculation was present within the exit region and there was a strong shear layer above the valley at gap level, with the above-ridge flow only slightly dipping into the valley (Fig. 12). In numerical and laboratory studies, this case lies within the total blocking regime (Fig. 1), which is consistent with observations.

c. *Case 3: Intermediate G*

In addition to the very low and high G_c cases discussed above, two moderately stratified cases with $G_c \sim O(1)$ were studied.

The case of $G_c = 1.4$ is shown in Figs. 13 and 14 . Here, both G_t (1.6) and G_e (1.2) are of the same order as G_c, indicating a balance between buoyant and inertial forces within the lower air column. As expected, there existed low-level upstream deflection parallel to the ridge (southeasterly flow in Fig. 13a)

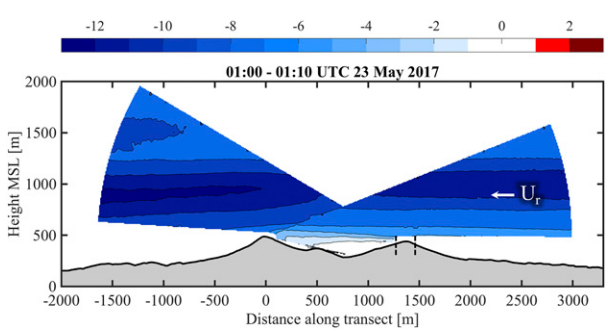

FIG. 8. Case 1: as in Fig. 6, but for the period with $G_c = 0.8$.

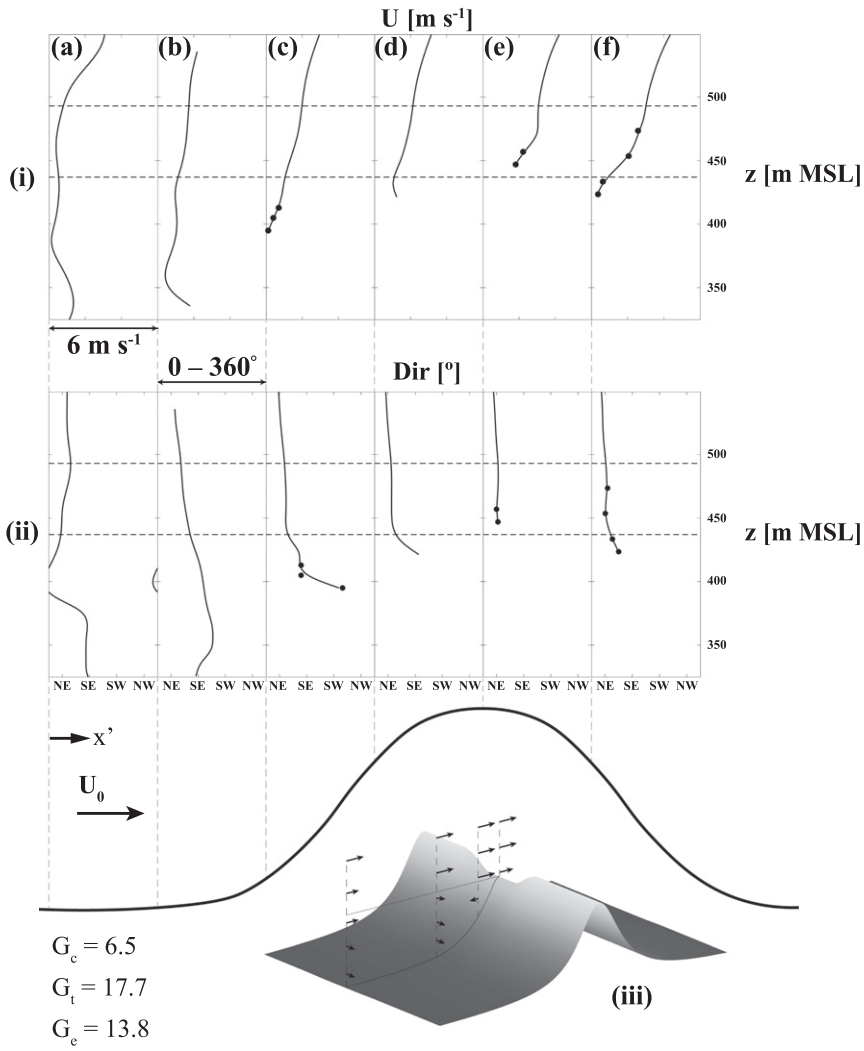

FIG. 9. Case 2: as in Fig. 5, but for the period with $G_c = 6.5$.

and stronger acceleration within the gap (compared to the case 1 flows). Ridge-normal northeasterly flow persisted throughout the gap passage, with maximum flow enhancement of $\sim 2.25U_0$ at the gap exit (Fig. 18d). Previous studies on flow over a single hill described $G \approx 1.4$ as a mountain wave regime where downstream flow follows the lee slope and generates flow subsidence (Gaberšek and Durran 2004). While wave signatures were evident (Fig. 14), neither trapped wave features nor significant subsidence was apparent from the tower and lidar data, likely due to destructive wave interference induced by the southern ridge (Stiperski et al. 2017; Gyüre and Jánosi 2003). There instead existed a low-level region of southerly valley flow. The presence of the valley and a second (southern) ridge likely had a significant effect on the exiting gap flow in this regime.

The case with $G_c = 1.3$ is shown in Figs. 15 and 16 . Both G_e and G_t are also $O(1)$, leading to mild upstream flow splitting. However, splitting near ground level is minimized as low-level convective heating during this period (Fig. 4b) likely causes a weak anabatic flow that ascends along the slope [although flow above is still stably stratified; morning transition mechanisms are detailed by Princevac and Fernando (2008)]. The flow at the gap height accelerates as it approaches and passes through

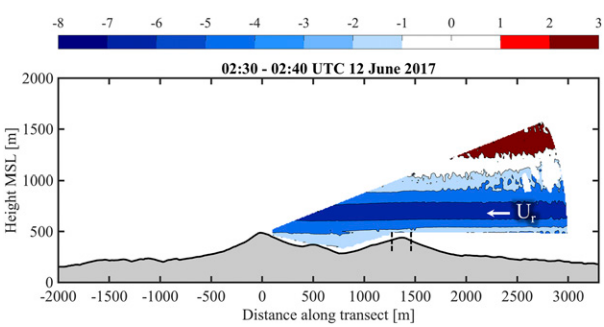

FIG. 10. Case 2: as in Fig. 6, but for a single scanning lidar on the southern ridge for the period with $G_c = 6.5$.

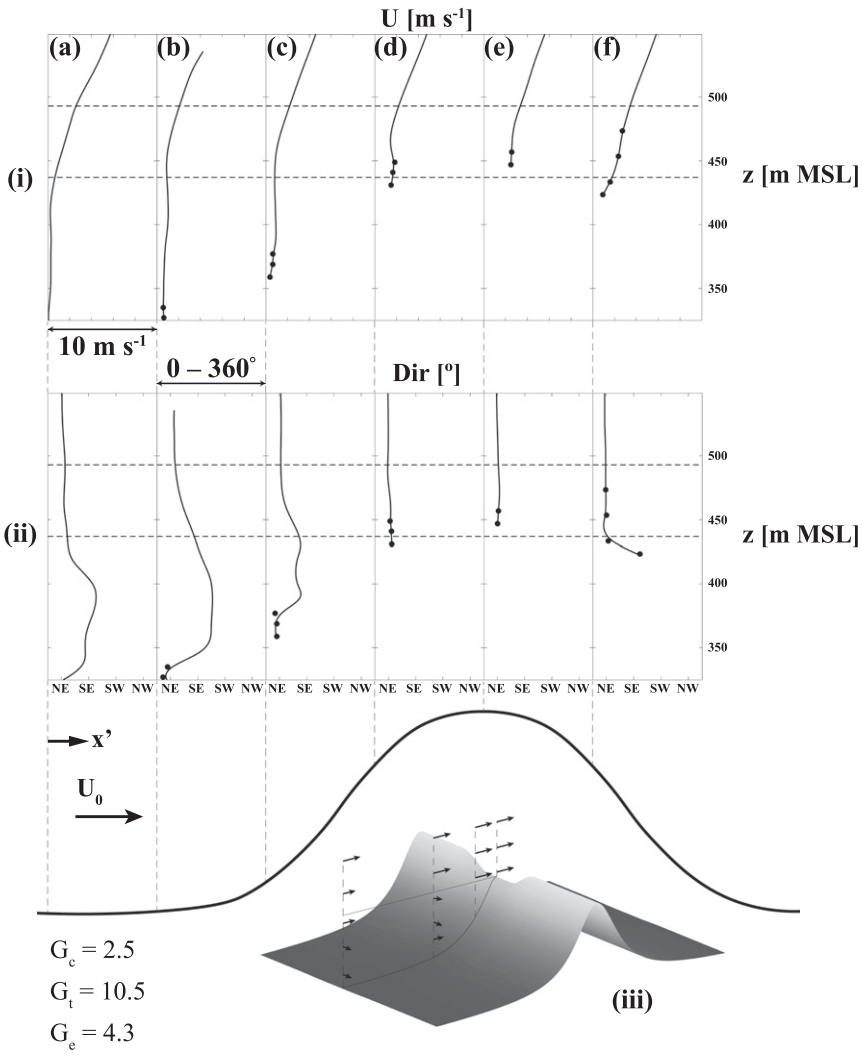

FIG. 11. Case 2: as in Fig. 5, but for the period with $G_c = 2.5$.

the gap, leading to flow enhancement of $\sim 2U_0$ near ground level within the gap (Fig. 17). Similar to the case with $G_c = 1.4$, this case is characterized by a lack of wave activity (Fig. 16) and southerly valley flow near ground level at the gap exit (Fig. 15f). Unlike all other observed cases, very high flow enhancement can be seen more than 100 m above the northern ridge ($z^*/h_c \gtrsim 1.7$ in Fig. 18c) as the upstream jet appears to thicken as it approaches and passes over the double-ridge topography (dark blue region expanding from right to left in Fig. 16).

5. Discussion

While the gap flow configuration studied here is ostensibly an extension of previous investigations of flow over hills, detailed flow regimes identified using nondimensional mountain height remain somewhat ambiguous. One major difficulty lies in the reconciliation with major previous gap flow studies, notably the numerical studies of Saito (1993), Zängl (2002), and Gaberšek and Durran (2004). Configurational discrepancies between these studies have led to disparities between calculated flow patterns and, therefore, the studies' conclusions. Additionally, such numerical studies usually utilize canonical density and velocity profiles (e.g., uniform flow,

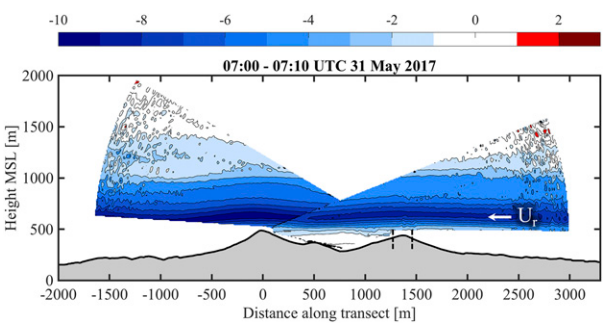

FIG. 12. Case 2: as in Fig. 6, but for the period with $G_c = 2.5$.

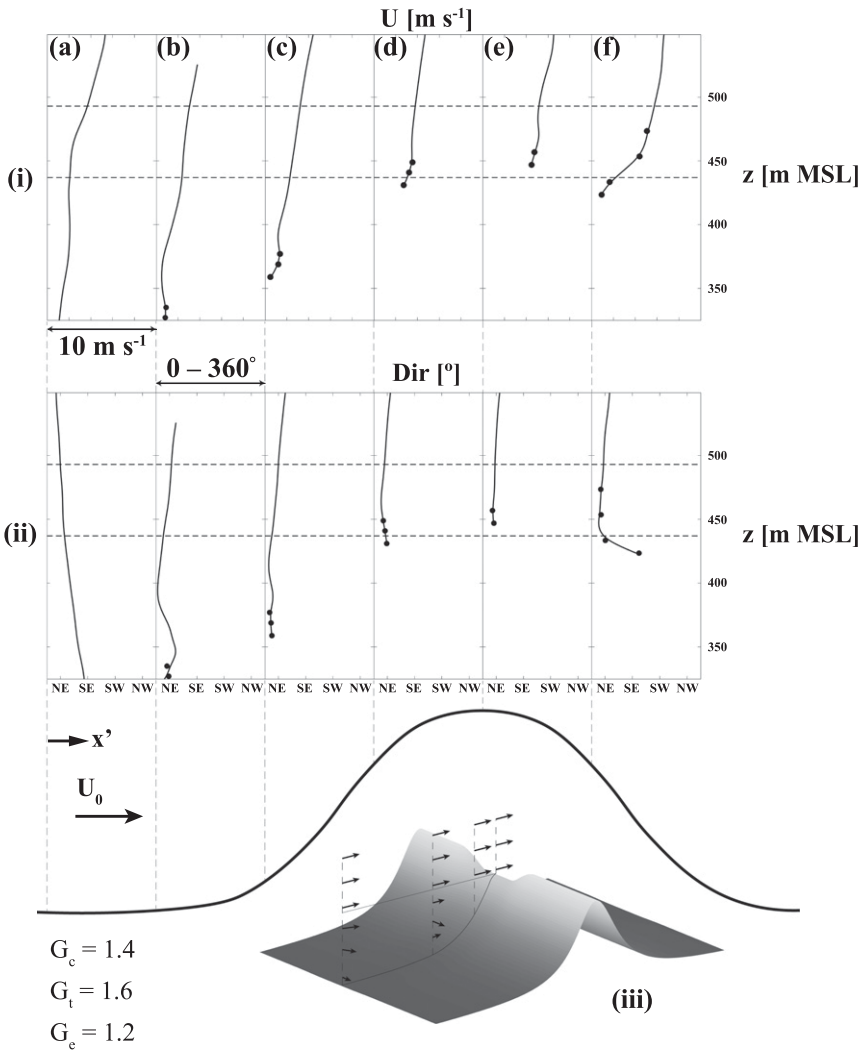

FIG. 13. Case 3: as in Fig. 5, but for the period with $G_c = 1.4$.

constant buoyancy frequency or simple variations thereof), and thus direct comparison with field observations is challenging.

The governing parameter for uniform flow (with constant buoyancy frequency) past a hill is $G = Nh/U_0$, and the presence of a ridge gap introduces additional parameters such as gap aspect ratios and topographic shape. Topographic parameters for a given study remain invariant but vary between locations, thus precluding the portability of results. To address the vertical variability of N and U profiles, we employed three parameters: G_c (30-min averaged G values calculated using N and U_0 measured upstream over the gap height), G_t (the local G obtained as above, averaged from the ground to the ridge height), and an equivalent G (G_e) calculated based on simple energetics used in dividing streamline analysis. Our observations, together with those of previous numerical single-hill gap flow studies, suggest that flow past topography with a gap can be broadly classified into three regimes based on G_c, while variations within a given regime may be interpreted using G_t and/or G_e. The main regimes identified are $G_c < 1$ (regime 1), $G_c \sim O(1)$ (regime 2) and $G_c > O(1)$ (regime 3). Given the limited data availability, reckoning the demarcations between the regimes was not possible. Also note that the above numerical studies have not considered the presence of a second mountain, which has been shown to have an effect at least on

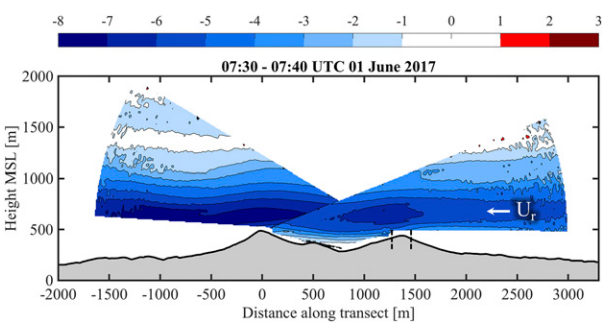

FIG. 14. Case 3: as in Fig. 6, but for the period with $G_c = 1.4$.

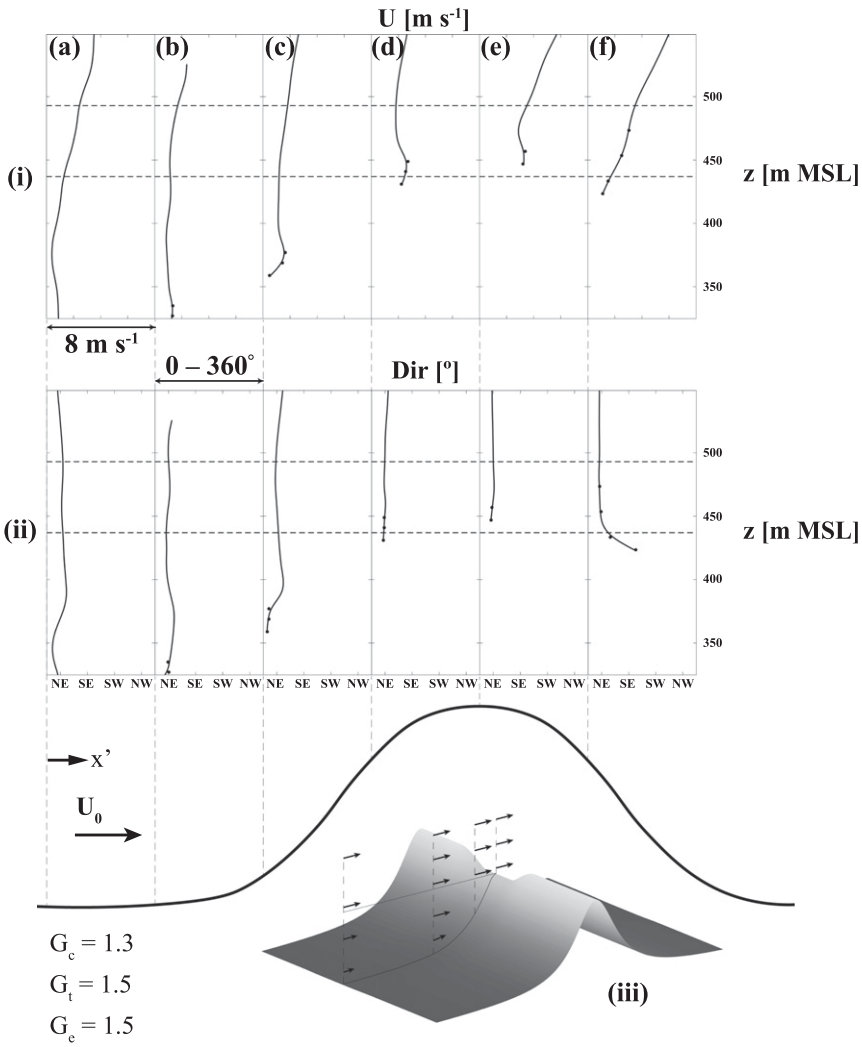

FIG. 15. Case 3: as in Fig. 5, but for the period with $G_c = 1.3$.

the lee wave patterns (Gyüre and Jánosi 2003; Stiperski and Grubišić 2011).

Regime 1 encompasses the weak stratification and/or high wind cases wherein the gap flow may undergo modest amplification, but no sharp jet-like acceleration profiles are found in the gap (thin solid and dashed lines in Fig. 17). At low G_c values ($G_c < 0.5$), the velocity amplification extends beyond the gap height, possibly because of higher turbulence (Reynolds stress) levels observed at lower G_c that facilitates vertical momentum transfer (not shown). Because no vertically propagating waves are expected in regime 1, no favorable pressure gradient due to wave drag exists to aid the gap flow, and thus it is expected to be governed by the (synoptic) background pressure gradient. As G_c increases, the flow transitions from a system that is external pressure gradient-driven to a system more associated with internal wave drag as discussed in section 2, causing gap flow amplification. The periods with G_c values of 0.3 and 0.8 belong to this regime, but the details of flow structures differ due to disparate G_t and G_e between the cases. The period with $G_c = 0.3$ displays smaller G_e and G_t values (both 0.7). According to Weissmann et al. (2004), weak lateral deflection is expected for this case, with flow turning gradually to match the mesoscale flow aloft. A majority of the flow rises along the windward slope and accelerates while freely passing through

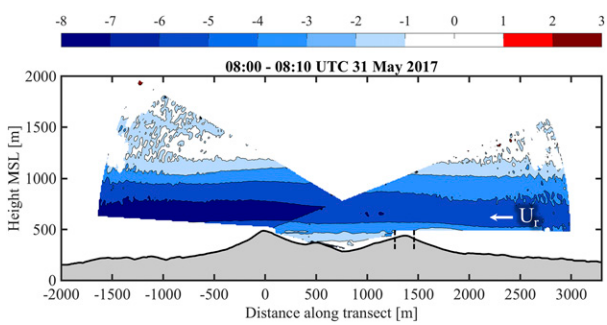

FIG. 16. Case 3: as in Fig. 6, but for the period with $G_c = 1.3$.

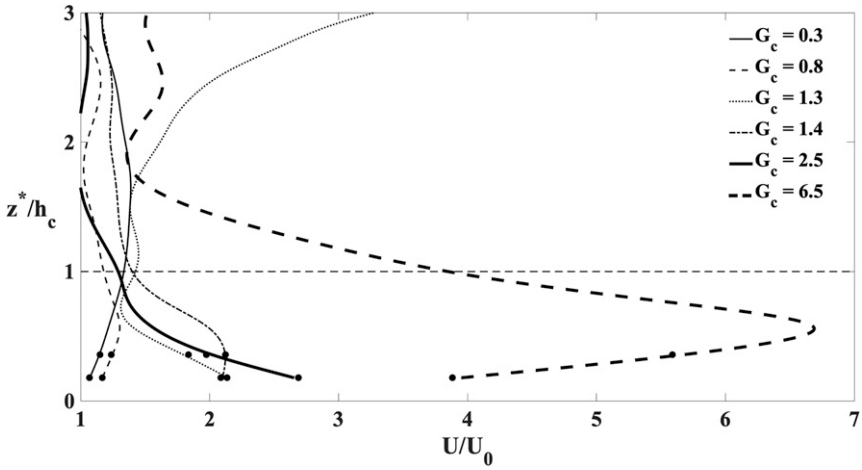

FIG. 17. Normalized wind speed in the center of the gap for all six time periods. The horizontal dashed line represents ridge height, while $z^*/h_c = 0$ represents the gap base. Black dots represent tower measurements that have been combined with the lidar measurements above to create the spline. U and U_0 are taken at the same elevation MSL.

the gap. For the periods with $G_c = 0.8$, moderate values of G_e (1.3) and G_t (6.6) suggest low wind speeds and/or enhanced stratification near the ground, making it difficult for the streamlines to rise and flow through the gap. As such, lateral flow deflection occurs over the windward slope.

Numerical simulations of Gaberšek and Durran (2004) suggest that, except for wide gaps, mass flux through the gap is dependent upon G. Because triple Doppler lidar velocity profiles were measured along the gap axis, the above result could be verified by calculating the total flow volume per unit width along the gap centerline and integrating over the gap height assuming the flow is predominantly horizontal in the region of the calculation (which was verified by measurements). Table 2 shows volume flux normalized by the approach volume flow rate at the S/R location. Given the flow variability upstream of the gap entrance, consideration of volume flux from gap entrance to exit is more appropriate when comparing the data with simulations of Gaberšek and Durran (2004). The volume flux from gap entrance to exit was constant and nearly independent of G in regime 1. This suggests passing of flow through the gap without much entrainment from above. A clear increase of volume flux from gap entrance to exit was evident for regime 2 (an increase of 40%–50%) and regime 3 (60%–85%), indicating flow subsidence (entrainment) into the gap from above. It is also interesting how the volume flux changed from the foothills to gap entrance over the windward face, which is a transition region from upstream flow to the gap. For regime 1, the change of this volume flux is less than ~7% suggesting that approach flow is not significantly modified and (a slab of) upstream flow continues to pass through the gap with some adjustments (see Figs. 5 and 7). In regime 2, however, the volume flux increases from the foothill to gap entrance by ~30%–50%, indicating significant flow adjustment over the windward face. This is possibly due to the stratification effects, in particular, upward flow convergence to the gap from the region between the gap height and the dividing streamline and lateral flow convergence. This is consistent with the tendency for jet-like acceleration at the gap entrance (Figs. 18c,d). In regime 3 a moderate change of volume flux from the foothills to gap entrance is noted (10%–20%), consistent with significant upstream blocking, meager upward flow convergence at the base of gap entrance (in contrast to regime 2), upstream streamlines passing through the gap opening without deflection (slab flow), and possible lateral flow convergence at the gap edges.

The numerical work of Saito (1993) indicated that, for nearly neutral flows ($G_c = 0.1$, corresponding to regime 1), the gap exit velocity is smaller than that in the vicinity of the peak of a contiguous ridge. Figure 18 shows the development of velocity profiles as the flow approaches ($x' < 1$), passes through ($x' = 1$) and exits ($x' > 1$) the gap for all study cases. Figure 19 shows the profiles over both the gap and a typical section of the ridge away from the gap for selected cases (lidar data at this location was unavailable for the $G_c = 6.5$ period; z' indicates the elevation above the ridge at a given measurement location). These measurements were taken by a profiling lidar on the northern ridge ~600 m SE of the gap. A comparison of the $G_c = 0.3$ profiles in Fig. 19a shows that the velocity on the ridge away from the gap is indeed higher than that within the gap. As G_c approaches 1 (Fig. 19b), the maximum flow acceleration over the typical ridge section is almost equivalent to the maximum acceleration over the gap. This coincides with a (presumed) ascension of the dividing streamline to higher elevations as G increases.

Flow in regime 2 shows clear localized flow enhancement within the gap which is distinct from that above the ridgeline ($z^*/h_c = 1$). Periods with $G_c = 1.3$ and $G_c = 1.4$ are representative of this regime, where the flow amplifies by a factor of ~2 through the gap (Figs. 18c,d). For both periods, the moderate G_e and G_t values indicate the presence of mild low-level flow deflection. At the gap level, the flow direction is largely unaffected by the topography. The volume flow rate follows a

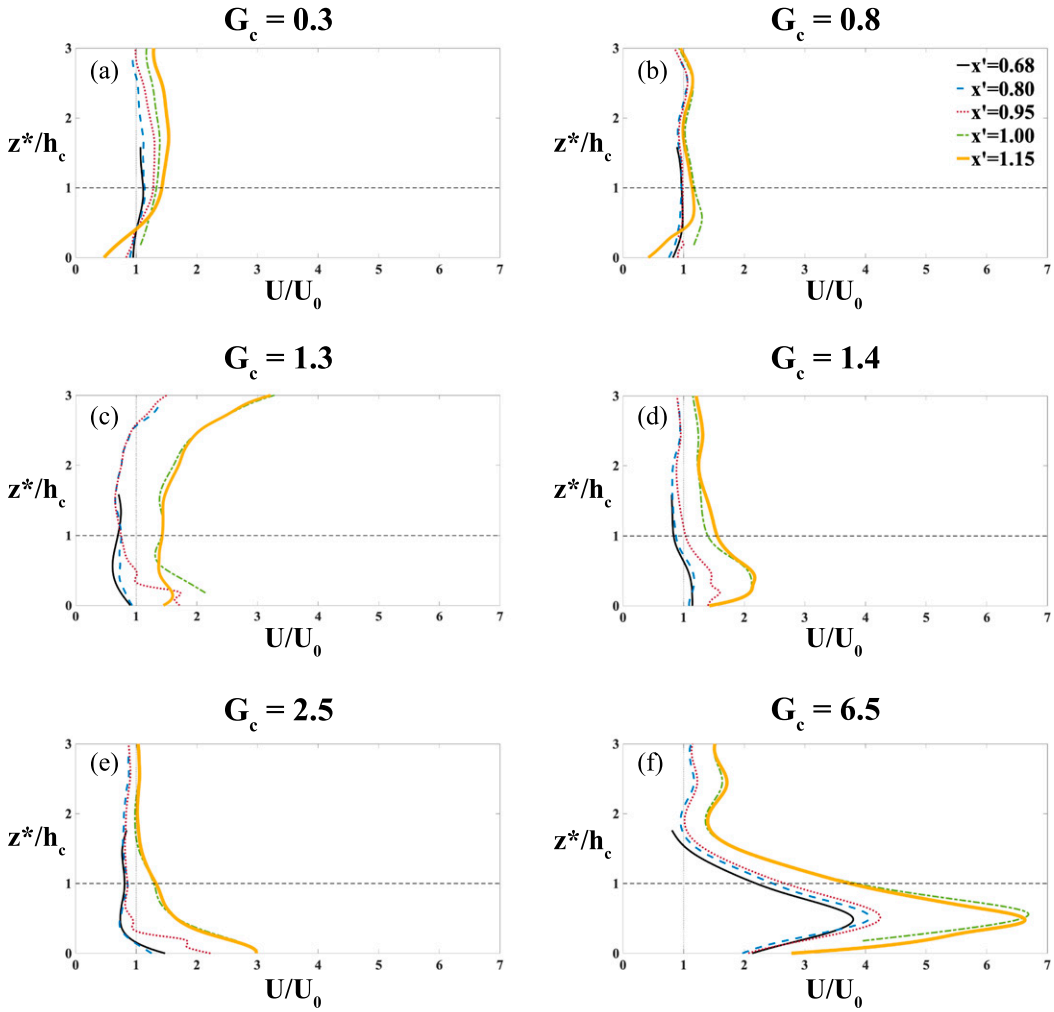

FIG. 18. Normalized wind speed for flow approaching, within, and just downstream of the gap, as denoted by $x' < 1$, $x' = 1$, and $x' > 1$, respectively. The horizontal dashed line represents ridge height, while $z^*/h_c = 0$ represents the elevation of the gap base.

similar pattern as that seen in Gaberšek and Durran (2004), with a modest increase in the upstream (only ~10% between foothills and the windward face) then considerably increasing from the windward face to gap entrance and then through the gap. This is likely due to vertical and lateral flow convergence at the gap entrance as well as flow subsidence along the entire gap, a phenomena observed by Gaberšek and Durran (2004), Marić and Durran (2009), and Overland and Walter (1981).

The work of Saito (1993), Zängl (2002), and Gaberšek and Durran (2004) indicate that trapped internal waves, wave breaking, flow splitting, partial blocking, and maximum speeds followed by a downstream hydraulic jump are all characteristics of regime 2, some of which are demonstrated by our observations. As G increases to ~1.5, Gaberšek and Durran (2004) predicted the appearance of a mountain wave regime with monotonic flow acceleration and a particularly strong increase in mass flux through the gap; because of the presence

TABLE 2. Normalized volume flow rates ($m^3 s^{-1}$) for each period with the corresponding G_c value.

G_c	Regime	Foothills	Windward face	Gap entrance	Gap center	Gap exit
0.3	1	1.03	1.04	1.07	1.09	1.05
0.8	1	0.95	0.91	0.94	1.12	0.98
1.3	2	0.68	0.77	1.03	1.47	1.46
1.4	2	1.03	1.07	1.32	1.71	1.97
2.5	3	0.87	0.85	1.06	1.63	1.95
6.5	3	3.09	3.17	3.44	4.82	5.45

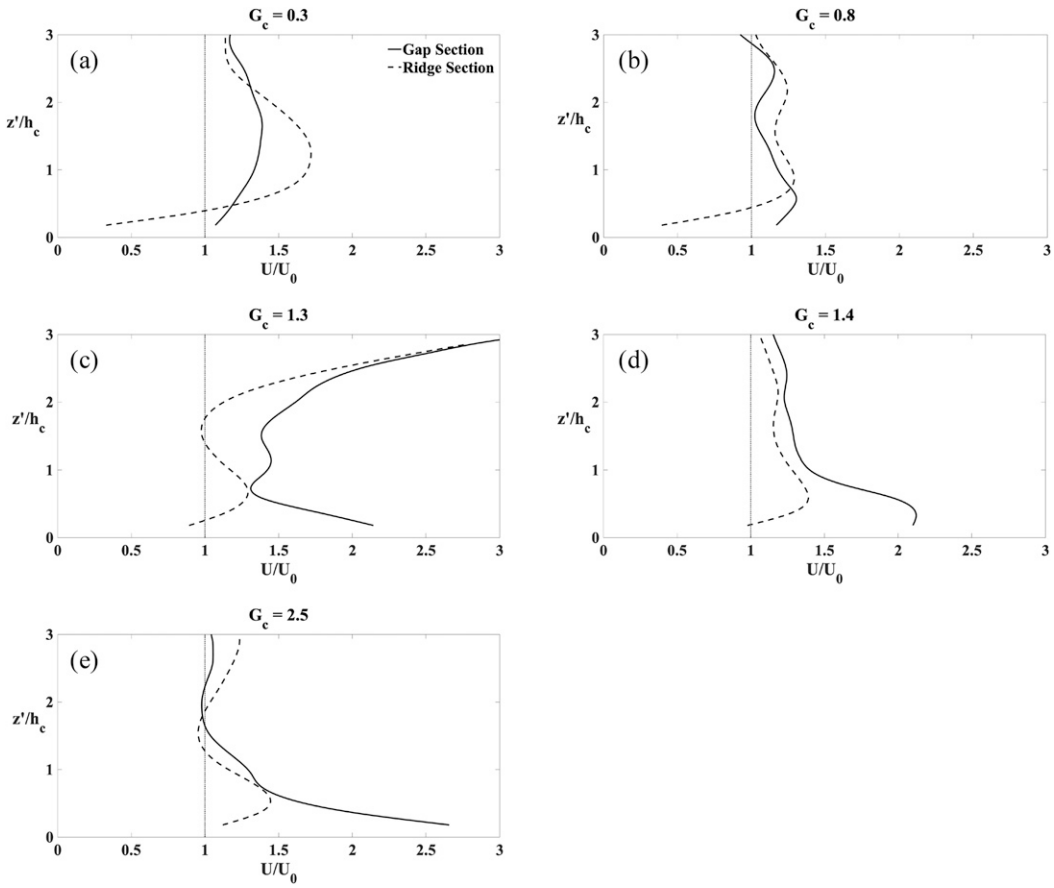

FIG. 19. Comparison of flow acceleration over the gap to that over a typical region of the northern ridge without a gap during select time periods. Necessary lidar data (from the typical section of the northern ridge) was unavailable for the period with $G_c = 6.5$. $z'/h_c = 0$ represents flow at surface level.

of lee waves, strong subsidence in the lee contributes to this increase. Observations shown in Figs. 18c and 18d are consistent with this trend and illustrate flow acceleration at the gap entrance and midpoint. Downstream acceleration was likely reduced (compared to that seen in previous studies) due to the topographic influence of the downstream ridge, which likely impeded mountain wave formation and steepening, thereby reducing flow subsidence at the gap exit (Gyüre and Jánosi 2003; Stiperski and Grubišić 2011). In this regime, flow acceleration over a typical section of the ridge was less than that seen within the gap, particularly near the surface level (Figs. 19c,d).

Flow in regime 3 ($G_c = 2.5$ and 6.5 cases) is characterized by relatively strong stratification and/or weak winds. Velocity profiles shown in Figs. 9(i)a–c and 11(i)a–c show nearly stagnant low-level upstream flow, but a steady increase of flow velocity above the elevation of the gap base. Flow within the gap accelerates and amplifies by a factor of at least 3 times (and up to 7 times) that seen at the S/R location. Gaberšek and Durran (2004) showed that such high G_c values indicate the restriction of vertical motion, causing flow to laterally converge into the gap, as fluid parcels outside the gap but at the gap's elevation can only flow laterally through the gap (and around the edges of the hill, if permitted). This is clearly evident from the marked increase of volume flow rate from the windward to lee side (Table 2). Winters and Armi (2014) showed that the jet profile is facilitated by the detachment of gap-level flow from the ground below, which is consistent with the observations of both cases. However, unlike that described in Marić and Durran (2009), the gap flow in our case was not completely detached from and stronger than the flow aloft, perhaps because the relatively small nondimensional gap height (~0.25) prevents complete gap flow detachment. According to Zängl (2002), regime 3 is fully blocked and also includes upstream flow splitting, lee waves, and a pressure gradient across the gap due to the high-drag state. Saito (1993) showed that winds in the gap's lee are stronger than in that of a typical section of the mountain away from the gap. These findings are generally consistent with our observations (Figs. 18e,f), although lee waves are likely suppressed by the downstream ridge (Gyüre and Jánosi 2003; Stiperski and Grubišić 2011). Large values of G_e and G_t are indicators of strong stratification and/or weak upstream winds, which induces strong flow splitting and possible flow reversal.

6. Conclusions

This investigation is the first comprehensive field study of microscale gap flows. Meteorological towers, a sodar/RASS

TABLE A1. Topographic parameters alongside their respective definitions.

Parameter	Definition
W	Gap width (along-ridge; $W \sim 700$ m)
L	Gap length (cross-ridge; $L \sim 100$ m)
h	Ridge height ($h \sim 250$ m)
h_c	Gap height ($h_c \sim 60$ m)
V	Valley width ($V \sim 1.5$ km)
z_s	Dividing streamline height
z^*	Height above the gap base
z'	Elevation above the ridge at a given measurement location

system, radiosonde launches, scanning lidars, and both a double and triple Doppler lidar system were utilized to map the characteristics of stratified flow passing through a microscale gap in a hill of double-ridge configuration, with approach flow normal to the ridges. Thirty-minute periods were analyzed which displayed different stable atmospheric conditions, and a gap-averaged nondimensional height G_c was utilized to categorize flow into three stably stratified regimes. Regime 1 ($G_c < 1$) is a nearly neutral flow regime wherein the gap has minimal effects on the surrounding flow field. Regime 2 [$G_c \sim O(1)$] is a transitional mountain wave regime wherein increasing internal wave drag and related buoyancy effects induce gap flow amplification. Regime 3 occurs when $G_c > O(1)$ and is associated with jetting gap flows that are completely distinct from the flow above. Upstream flow characteristics such as flow splitting and blocking/reversal are largely determined by G_e, the equivalent nondimensional mountain height for a fluid parcel near the ground level.

The findings of this study in general corroborate the results of earlier studies, particularly the numerical findings of Saito (1993), Gaberšek and Durran (2004), and Zängl (2002), although details vary considerably. This study's largest deviation from previous investigations is the partitioning of the traditional nondimensional height G into multiple categories to help better characterize flow phenomena; G_c indicates the ability of a fluid parcel to ascend past the gap height in order to rise above the ridge, whereas G_t and G_e are two separate indicators of the ability of an upstream fluid parcel near the ground level to rise above the ridge. Both of the latter G values account for the enhanced stratification and lower wind speeds at the ground level of a stably stratified atmospheric boundary layer and therefore are more representative of upstream conditions.

The three regimes described in this study generally align with those found in previous studies, although the specific demarcations between flow regimes and detailed flow structures identified in different studies cannot be rigorously compared because of the differences in flow configurations. While microscale topographic features are not resolved or parameterized in numerical weather models, this study shows that such features can have noticeable effects on flow fields upstream, downstream, and adjacent to the gap. Accounting for gap features through improved representation of subgrid processes may improve the predictive power of both mesoscale and microscale models.

Acknowledgments. This work was funded by the National Science Grants AGS-1565535 and AGS-1921554, and Wayne and Diana Murdy Endowment and Dean's Graduate Fellowship Program at the University of Notre Dame. The triple Lidar system was funded by the Defense University Research Instrumentation Program (DURIP) under the Office of Naval Research Grant N00014-15-1-2852. Special thanks to Dr. Chris Hocut and Ed Creegan of Army Research Laboratory for providing dual-Doppler lidar data, and various members of the National Center for Atmospheric Research, Danish Technical University, and University of Porto for collecting and processing the tower data. The authors would also like to thank the citizens of Vale do Cobrão for their hospitality and support during the extensive field campaign.

Data availability statement. All data from the Perdigão campaign is publicly available and may be found at any of the following sites: UPORTO (http://perdigao.fe.up.pt), United States (www.eol.ucar.edu/field_projects/Perdigão), and EU (www.neweuropeanwindatlas.eu).

APPENDIX

Topographic Parameters

A list of topographic parameters is given in Table A1. Likewise, Fig. A1 provides an illustrative diagram of the various topographic parameters utilized.

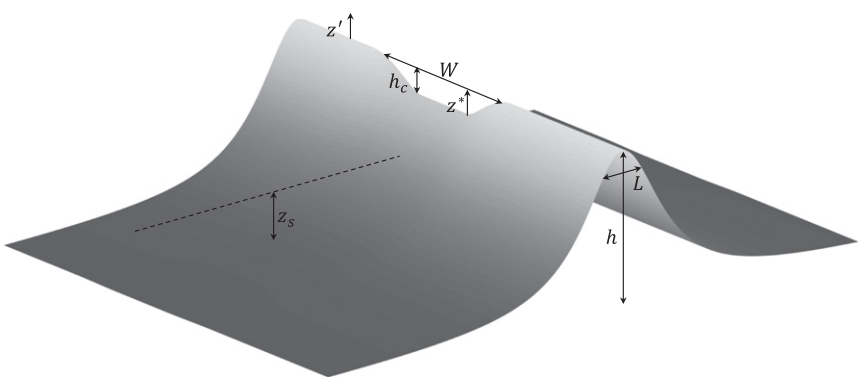

FIG. A1. Illustrative diagram of the various topographic parameters referenced.

REFERENCES

Baines, P. G., 1979: Observations of stratified flow past three-dimensional barriers. *J. Geophys. Res.*, **84**, 7834–7838, https://doi.org/10.1029/JC084iC12p07834.

——, 1987: Upstream blocking and airflow over mountains. *Annu. Rev. Fluid Mech.*, **19**, 75–95, https://doi.org/10.1146/annurev.fl.19.010187.000451.

——, 1998: *Topographic Effects in Stratified Flows*. Cambridge University Press, 500 pp.

——, and K. P. Hoinka, 1985: Stratified flow over two-dimensional topography in fluid of infinite depth: A laboratory simulation. *J. Atmos. Sci.*, **42**, 1614–1630, https://doi.org/10.1175/1520-0469(1985)042<1614:SFOTDT>2.0.CO;2.

Blumen, W., 2016: *Atmospheric Processes Over Complex Terrain*. Springer, 323 pp.

Boyer, D., P. Davies, H. Fernando, and X. Zhang, 1989: Linearly stratified flow past a horizontal circular cylinder. *Philos. Trans. Roy. Soc. London*, **328A**, 501–528, https://doi.org/10.1098/rsta.1989.0049.

Brighton, P., 1978: Strongly stratified flow past three-dimensional obstacles. *Quart. J. Roy. Meteor. Soc.*, **104**, 289–307, https://doi.org/10.1002/qj.49710444005.

Calhoun, R., R. Heap, M. Princevac, R. Newsom, H. Fernando, and D. Ligon, 2006: Virtual towers using coherent Doppler lidar during the Joint Urban 2003 dispersion experiment. *J. Appl. Meteor. Climatol.*, **45**, 1116–1126, https://doi.org/10.1175/JAM2391.1.

Choukulkar, A., and Coauthors, 2017: Evaluation of single and multiple Doppler lidar techniques to measure complex flow during the XPIA field campaign. *Atmos. Meas. Tech.*, **10**, 247–264, https://doi.org/10.5194/amt-10-247-2017.

Chow, F. K., S. F. De Wekker, and B. J. Snyder, 2013: *Mountain Weather Research and Forecasting: Recent Progress and Current Challenges*. Springer, 750 pp.

Clarke, A. J., 1988: Inertial wind path and sea surface temperature patterns near the Gulf of Tehuantepec and Gulf of Papagayo. *J. Geophys. Res.*, **93**, 15 491–15 501, https://doi.org/10.1029/JC093iC12p15491.

Colle, B., and C. Mass, 2000: High-resolution observations and numerical simulations of easterly gap flow through the Strait of Juan de Fuca on 9-10 December 1995. *Mon. Wea. Rev.*, **128**, 2398–2422, https://doi.org/10.1175/1520-0493(2000)128<2398:HROANS>2.0.CO;2.

Dorman, C., R. Beardsley, and R. Limeburner, 1995: Winds in the Strait of Gibraltar. *Quart. J. Roy. Meteor. Soc.*, **121**, 1903–1921, https://doi.org/10.1002/qj.49712152807.

Fernando, H., and Coauthors, 2019: The Perdigão: Peering into microscale details of mountain winds. *Bull. Amer. Meteor. Soc.*, **100**, 799–819, https://doi.org/10.1175/BAMS-D-17-0227.1.

Finnigan, T. D., J. A. Vine, P. L. Jackson, S. E. Allen, G. A. Lawrence, and D. G. Steyn, 1994: Hydraulic physical modeling and observations of a severe gap wind. *Mon. Wea. Rev.*, **122**, 2677–2687, https://doi.org/10.1175/1520-0493(1994)122<2677:HPMAOO>2.0.CO;2.

Gaberšek, S., and D. Durran, 2004: Gap flows through idealized topography, Part I: Forcing by large-scale winds in the nonrotating limit. *J. Atmos. Sci.*, **61**, 2846–2862, https://doi.org/10.1175/JAS-3340.1.

——, and D. R. Durran, 2006: Gap flows through idealized topography. Part II: Effects of rotation and surface friction. *J. Atmos. Sci.*, **63**, 2720–2739, https://doi.org/10.1175/JAS3786.1.

Gill, A. E., 1982: *Atmosphere-Ocean Dynamics*. Academic Press, 662 pp.

Grubišić, V., and I. Stiperski, 2009: Lee-wave resonances over double bell-shaped obstacles. *J. Atmos. Sci.*, **66**, 1205–1228, https://doi.org/10.1175/2008JAS2885.1.

Gyüre, B., and I. M. Jánosi, 2003: Stratified flow over asymmetric and double bell-shaped obstacles. *Dyn. Atmos. Oceans*, **37**, 155–170, https://doi.org/10.1016/S0377-0265(03)00030-7.

Houghton, D. D., and A. Kasahara, 1968: Nonlinear shallow fluid flow over an isolated ridge. *Commun. Pure Appl. Math.*, **21** (1), 1–23, https://doi.org/10.1002/cpa.3160210103.

Jackson, P., and D. G. Steyn, 1994: Gap winds in a fjord. Part I: Observations and numerical simulation. *Mon. Wea. Rev.*, **122**, 2645–2665, https://doi.org/10.1175/1520-0493(1994)122<2645:GWIAFP>2.0.CO;2.

Kaimal, J. C., and J. J. Finnigan, 1994: *Atmospheric Boundary Layer Flows: Their Structure and Measurement*. Oxford University Press, 289 pp.

Klemp, J., and D. Lilly, 1975: The dynamics of wave-induced downslope winds. *J. Atmos. Sci.*, **32**, 320–339, https://doi.org/10.1175/1520-0469(1975)032<0320:TDOWID>2.0.CO;2.

Leo, L. S., M. Y. Thompson, S. Di Sabatino, and H. J. Fernando, 2016: Stratified flow past a hill: Dividing streamline concept revisited. *Bound.-Layer Meteor.*, **159**, 611–634, https://doi.org/10.1007/s10546-015-0101-1.

Lin, Q., W. Lindberg, D. Boyer, and H. Fernando, 1992: Stratified flow past a sphere. *J. Fluid Mech.*, **240**, 315–354, https://doi.org/10.1017/S0022112092000119.

Long, R. R., 1952: The flow of a liquid past a barrier in a rotating spherical shell. *J. Meteor.*, **9**, 187–199, https://doi.org/10.1175/1520-0469(1952)009<0187:TFOALP>2.0.CO;2.

——, 1953: Some aspects of the flow of stratified fluids: I. A theoretical investigation. *Tellus*, **5**, 42–58, https://doi.org/10.3402/tellusa.v5i1.8563.

Lundquist, J. K., M. Churchfield, S. Lee, and A. Clifton, 2015: Quantifying error of lidar and sodar Doppler beam swinging measurements of wind turbine wakes using computational fluid dynamics. *Atmos. Meas. Tech.*, **8**, 907–920, https://doi.org/10.5194/amt-8-907-2015.

——, and Coauthors, 2017: Assessing state-of-the-art capabilities for probing the atmospheric boundary layer: The XPIA field campaign. *Bull. Amer. Meteor. Soc.*, **98**, 289–314, https://doi.org/10.1175/BAMS-D-15-00151.1.

Mann, J., and Coauthors, 2017: Complex terrain experiments in the New European Wind Atlas. *Philos. Trans. Roy. Soc.*, **375A**, 20160101, https://doi.org/10.1098/rsta.2016.0101.

Marić, T., and D. R. Durran, 2009: Observations of gap flow in the Wipp Valley on 20 October 1999: Evidence of subsidence. *J. Atmos. Sci.*, **66**, 984–1001, https://doi.org/10.1175/2008JAS2568.1.

Mayr, G. J., and Coauthors, 2004: Gap flow measurements during the Mesoscale Alpine Programme. *Meteor. Atmos. Phys.*, **86**, 99–119, https://doi.org/10.1007/s00703-003-0022-2.

Menke, R., J. Mann, and N. Vasiljevic, 2018: Perdigão-2017: Multi-lidar flow mapping over the complex terrain site. Technical University of Denmark, accessed 13 July 2020, https://doi.org/10.11583/DTU.7228544.v1.

——, N. Vasiljević, J. Mann, and J. K. Lundquist, 2019: Characterization of flow recirculation zones at the Perdigão site using multi-lidar measurements. *Atmos. Chem. Phys.*, **19**, 2713–2723, https://doi.org/10.5194/acp-19-2713-2019.

Newsom, R. K., and R. Krishnamurthy, 2020: Doppler Lidar (DL) instrument handbook. Tech. Rep. DOE/SC-ARM/TR-101, Atmospheric Radiation Measurement (ARM) Program, 58 pp.

——, L. K. Berg, W. J. Shaw, and M. L. Fischer, 2015: Turbine-scale wind field measurements using dual-Doppler lidar. *Wind Energy*, **18**, 219–235, https://doi.org/10.1002/we.1691.

——, W. A. Brewer, J. M. Wilczak, D. E. Wolfe, S. P. Oncley, and J. K. Lundquist, 2017: Validating precision estimates in horizontal wind measurements from a Doppler lidar. *Atmos. Meas. Tech.*, **10**, 1229–1240, https://doi.org/10.5194/amt-10-1229-2017.

Overland, J., 1984: Scale analysis of marine winds in straits and along mountainous coasts. *Mon. Wea. Rev.*, **112**, 2530–2534, https://doi.org/10.1175/1520-0493(1984)112<2530:SAOMWI>2.0.CO;2.

——, and B. Walter, 1981: Gap winds in the Strait of Juan de Fuca. *Mon. Wea. Rev.*, **109**, 2221–2233, https://doi.org/10.1175/1520-0493(1981)109<2221:GWITSO>2.0.CO;2.

Pan, F., and R. Smith, 1999: Gap winds and wakes: SAR observations and numerical simulations. *J. Atmos. Sci.*, **56**, 905–923, https://doi.org/10.1175/1520-0469(1999)056<0905:GWAWSO>2.0.CO;2.

Pearson, G., F. Davies, and C. Collier, 2009: An analysis of the performance of the UFAM pulsed Doppler lidar for observing the boundary layer. *J. Atmos. Oceanic Technol.*, **26**, 240–250, https://doi.org/10.1175/2008JTECHA1128.1.

Politovich, M. K., R. K. Goodrich, C. S. Morse, A. Yates, R. Barron, and S. A. Cohn, 2011: The Juneau terrain-induced turbulence alert system. *Bull. Amer. Meteor. Soc.*, **92**, 299–313, https://doi.org/10.1175/2010BAMS3024.1.

Princevac, M., and H. Fernando, 2008: Morning breakup of cold pools in complex terrain. *J. Fluid Mech.*, **616**, 99–109, https://doi.org/10.1017/S0022112008004199.

Queney, P., 1948: The problem of air flow over mountains: A summary of theoretical studies. *Bull. Amer. Meteor. Soc.*, **29**, 16–26, https://doi.org/10.1175/1520-0477-29.1.16.

Reed, T. R., 1931: Gap winds of the Strait of Juan de Fuca. *Mon. Wea. Rev.*, **59**, 373–376, https://doi.org/10.1175/1520-0493(1931)59<373:GWOTSO>2.0.CO;2.

Saito, K., 1993: A numerical study of the local downslope wind ''Yamaji-kaze'' in Japan Part II: Non-linear aspect of the 3-D flow over a mountain ridge with a col. *J. Meteor. Soc. Japan*, **71**, 247–272, https://doi.org/10.2151/jmsj1965.71.2_247.

Scorer, R., 1952: Mountain-gap winds; A study of surface wind at Gibraltar. *Quart. J. Roy. Meteor. Soc.*, **78**, 53–61, https://doi.org/10.1002/qj.49707833507.

Sheppard, P., 1956: Airflow over mountains. *Quart. J. Roy. Meteor. Soc.*, **82**, 528–529, https://doi.org/10.1002/qj.49708235418.

Smith, R. B., 1980: Linear theory of stratified hydrostatic flow past an isolated mountain. *Tellus*, **32**, 348–364, https://doi.org/10.3402/tellusa.v32i4.10590.

Sprenger, M., and C. Schär, 2001: Rotational aspects of stratified gap flows and shallow föhn. *Quart. J. Roy. Meteor. Soc.*, **127**, 161–187, https://doi.org/10.1002/qj.49712757110.

Steenburgh, W. J., D. M. Schultz, and B. A. Colle, 1998: The structure and evolution of gap outflow over the Gulf of Tehuantepec, Mexico. *Mon. Wea. Rev.*, **126**, 2673–2691, https://doi.org/10.1175/1520-0493(1998)126<2673:TSAEOG>2.0.CO;2.

Stiperski, I., and V. Grubišić, 2011: Trapped lee wave interference in the presence of surface friction. *J. Atmos. Sci.*, **68**, 918–936, https://doi.org/10.1175/2010JAS3495.1.

——, and Coauthors, 2017: Water tank experiments on stratified flow over double mountain-shaped obstacles at high-Reynolds number. *Atmosphere*, **8**, 13, https://doi.org/10.3390/atmos8010013.

Trüb, J., and H. Davies, 1995: Flow over a mesoscale ridge: Pathways to regime transition. *Tellus*, **47A**, 502–524, https://doi.org/10.3402/tellusa.v47i4.11542.

Vasiljević, N., and Coauthors, 2017: Perdigão 2015: Methodology for atmospheric multi-Doppler lidar experiments. *Atmos. Meas. Tech.*, **10**, 3463–3483, https://doi.org/10.5194/amt-10-3463-2017.

Wang, Y., C. M. Hocut, S. W. Hoch, E. Creegan, H. J. Fernando, C. D. Whiteman, M. Felton, and G. Huynh, 2016: Triple Doppler wind lidar observations during the mountain terrain atmospheric modeling and observations field campaign. *J. Appl. Remote Sens.*, **10**, 026015, https://doi.org/10.1117/1.JRS.10.026015.

Weissmann, M. D., G. Mayr, R. Banta, and A. Gohm, 2004: Observations of the temporal evolution and spatial structure of the gap flow in the Wipp Valley on 2 and 3 October 1999. *Mon. Wea. Rev.*, **132**, 2684–2697, https://doi.org/10.1175/MWR2817.1.

Whiteman, C. D., 2000: *Mountain Meteorology: Fundamentals and Applications*. Oxford University Press, 355 pp.

Winters, K. B., and L. Armi, 2014: Topographic control of stratified flows: Upstream jets, blocking and isolating layers. *J. Fluid Mech.*, **753**, 80–103, https://doi.org/10.1017/jfm.2014.363.

Xu, X., and C. Yi, 2013: The influence of geometry on recirculation and CO_2 transport over forested hills. *Meteor. Atmos. Phys.*, **119**, 187–196, https://doi.org/10.1007/s00703-012-0224-6.

Zängl, G., 2002: Stratified flow over a mountain with a gap: Linear theory and numerical simulations. *Quart. J. Roy. Meteor. Soc.*, **128**, 927–949, https://doi.org/10.1256/0035900021643755.

Copyright of Journal of the Atmospheric Sciences is the property of American Meteorological Society and its content may not be copied or emailed to multiple sites or posted to a listserv without the copyright holder's express written permission. However, users may print, download, or email articles for individual use.